Studies on optical properties of diesel exhaust particles

(ディーゼル排ガス粒子の光学特性の研究)

Guo Xuesong

郭　雪松

Contents

Symbols and abbreviations

λ	Wavelength
σ	Standard deviation
AAE	Absorption Ångström exponent
APM	Aerosol particle mass analyzer
b_{abs}	Absorption coefficients
b_{sca}	Scattering coefficients
BC	Black carbon
BrC	Brown carbon
CPC	Condensation particle counter
CVS	Constant volume sampler
DEP	Diesel exhaust particles
DMA	Differential mobility analyzer
DMS	Dimethyl sulfide
EC	Elemental carbon
GC	Gas chromatography
IPCC	Intergovernmental panel on climate change
IR	Infrared
LC-MS	Liquid chromatography-mass spectrometry
M_{EBC}	Mass concentrations of equivalent BC
M_{org}	Mass concentration of organics
MAC_{BC}	Mass absorption cross section for BC
M_{EC}	Mass concentration of EC
M_{TC}	Mass concentration of total carbon
M_{OM}	Mass concentration of OM
NFR	Number fraction remaining
NMVOC	Non-methane volatile organic compounds
OC	Organic carbon
OM	Organic matter
OSM	Organic-soluble material
PAS	Photoacoustic spectrometer
PASS-3	Three-wavelength photoacoustic soot spectrometer
PSAP	Particle soot absorption photometer

PTFE	Polytetrafluoroethylene
PTR-MS	Proton-transfer reaction mass spectrometry
PSL	Polystyrene latex
Q-AMS	Aerodyne quadrupole-based aerosol mass spectrometer
RF	Radiative forcing
RI	Refractive index
SMPS	Scanning mobility particle sizers
SOF	Soluble organic fraction
SSA	Single scattering albedo
TEM	Transmission electron microscope
THC	Total hydrocarbons
UV	Ultra-violet
VFR	Volume fraction remaining
VOCs	Volatile organic compounds
WSM	Water-soluble material

Abstract

Atmospheric particulate matter influences climate directly by scattering and absorbing incoming solar radiation. To identify and simulate the global warming problem, a detailed understanding of aerosol optical properties is required. Black carbon (BC) is an important component of global warming in terms of direct radiative forcing. Recently, a fraction of organic matter (OM) called brown carbon (BrC), was suggested to have the ability to absorb solar radiation at ultraviolet and shorter visible wavelengths. Additionally, enhancement of light absorption of BC due to coating with OM and inorganic materials, which is referred to as the lensing effect, is also reported. However, the contributions of BrC and the lensing effect are still not well understood. Diesel exhaust particles (DEP) are one of the main anthropogenic sources of BC and OM. Understanding the optical properties of DEP, including the enhancement of light absorption of BC due to coating and light absorption by OM, is important for evaluating the climate impact of DEP. In this study, a three-wavelength photoacoustic soot spectrometer (405, 532 and 781 nm) was used to investigate the wavelength-dependent optical properties of DEP emitted from a diesel engine vehicle running on a chassis dynamometer in transient driving mode (JE-05) and at a constant speed (either idling or driving at 70 km/h). Optical properties of the diluted exhaust were measured after it was passed through a heater, set at 20, 47 or 300°C (transient driving mode) or between 20 and 400°C (constant driving mode). The OM accounted for, on average, ~40% and ~35% of the total mass concentration of DEP during the transient and constant driving modes, respectively. In the transient driving mode, enhancements of scattering coefficients at 20 and 47°C, and of the mass concentration of organics, were observed during the high-speed driving period (~80 km/h) corresponding to driving on a highway. No difference was observed in the absorption coefficients between heated and unheated particles at 781 nm for either the transient (including the high-speed driving period) or constant driving modes. These results indicate a lack of enhancement due to the lensing effect, possibly because the BC was mainly mixed externally with the OM or because it was located at the edges of particles under these experimental conditions. Contributions to the total light absorption at 405 nm by the OM were estimated by comparing the wavelength dependence of the absorption coefficients with and without heating. A significant contribution by the light-absorbing OM (20% ± 7%) to the total light absorption at 405 nm was observed during the high-speed driving period of the JE-05 mode, while the contributions were small during other periods in the JE-05 mode

(0% ± 8%) and the constant driving mode (idling: 4% ± 12%; driving at 70 km/h: 0% ± 16%).

要旨

大気中に浮遊する微小粒子であるエアロゾルは、二酸化炭素などの温室効果気体とともに、放射収支を通じて地球の気候に影響をあたえると考えられている。エアロゾルによる太陽光の散乱は大気の冷却化、光吸収は大気の温暖化の直接的な効果を与える。地球温暖化の解明と将来予測を行う際には、エアロゾルの光学特性(消散・散乱・吸収)の詳細な理解が重要である。しかし、IPCC においては、現状ではエアロゾルの放射収支への影響の定量的な理解の不確定性が大きいと指摘されている。エアロゾルの光吸収に関しては、光吸収性エアロゾルとして、ブラックカーボン(BC)粒子が考慮されてきたが、近年、有機性炭素 (OC) のうちの短波長可視から紫外領域に光吸収性を有する「ブラウンカーボン」が、大気の放射収支や光化学過程に寄与を持つ可能性が指摘されている。また、BC が有機物および無機塩類のような物質に被覆されると、被覆物が「レンズ」のような効果を果たして BC の光吸収性が増加されることも予測されている。有機エアロゾルには、ディーゼル排ガスやバイオマス燃焼などから大気中に直接放出される一次有機エアロゾル(POA)と、産業活動や植物などから大気中に放出された揮発性有機化合物(VOC)が大気酸化反応を経て粒子化し、生成する二次有機エアロゾル(SOA)がある。しかし、どのような有機エアロゾルが、どの程度の光吸収性を有するかについては、よくわかっていないのが現状である。本論文では、エアロゾルの光学特性を粒子が浮遊した状態で直接計測できる光音響分光(PAS)装置を用いた室内実験により、SOA やディーゼル排ガス粒子(DEP)中の有機炭素成分(OC)の光吸収特性について研究した。

交通安全環境研究所のシャシーダイナモ施設でディーゼルトラックを走行させ、排ガス粒子の光学特性を調べた。実験は、市街地での走行を想定した「過渡走行モード(JE05)」及び、車両を一定の速度で走行させる「等速走行モード(アイドリング, 70 km/h)」で行った。PAS 装置の上流にヒーターを取り付け、様々な温度条件下で、3 波長(405, 532, 781 nm)における吸収($b_{abs}(\lambda)$)および散乱係数($b_{sca}(\lambda)$)を測定した。実験の結果、過渡走行モードでは、高速走行(80 km/h 程度)前後の加減速時に、大きな散乱係数が観測された。粒子を 300℃に加熱した上で測定した場合には、散乱係数の増加が見られなかったことから、300℃で揮発する OC 成分がエンジンより排出されたと考えられる。加熱および非加熱時に得られた吸収係数の波長依存性から、OC による光吸収の 405 および 532 nm の全光吸収に対する寄与($b_{abs,OC}(\lambda)/b_{abs,total}(\lambda)$)を推定したところ、405 nm においては、過渡走行モードの高速走行時に 20%程度の寄与を有すること、532 nm においては 7%程度の寄与を見出した。ただし、レンズ効果による BC の光吸収の増加はほとんどなかったと分かった。一方、等速走行モードの実験では、高速走行(70 km/h)した場合においても、波長 405 nm での OC による光吸収の寄与は殆ど無いことを示した。これ

らの結果により、ディーゼルエンジン排ガス中のエアロゾルが大気の放射収支に与える影響を定量的に見積もるための重要な情報を提供した。

Chapter 1

Introduction

1.1. Radiative effect of aerosols

Atmospheric particulate matter, also called aerosol, plays a very important role in determining the visibility, health effects, heterogeneous chemistry, and radiation balance of the atmosphere on the local and global scales. Several phenomena occur when an aerosol particle is irradiated by light (Figure 1). Light absorption by aerosol transfers the energy of incident light into the internal energy of aerosol. In diffraction, the incident light resonates inside the aerosol and irradiated again. In reflection, the aerosol particles work as a mirror to reflect the incident light directly. Aerosol can also refract the incident light due to the difference in refraction index (RI) between aerosol and air. The sum of light diffraction, reflection and refraction is called light scattering, and the sum of light absorption and light scattering is called light extinction.

Aerosol particles come from a lot of sources, classified as direct emission and secondary formation. The emission sources of aerosol particles also emit gases (e.g. SO_2, volatile organic compounds (VOCs), dimethyl sulphide (DMS)). Photochemical reactions of these gases possibly generate aerosol particles. This process is called secondary formation. Aerosol particles influence both global and regional climate directly by scattering and absorbing incoming solar radiation and indirectly by acting as cloud condensation nuclei (Figure 2). To quantify the direct influence of direct emission and secondary formation on the atmosphere, the radiation balance should be calculated.

The Intergovernmental Panel on Climate Change (IPCC) reported that climate

models reproduce the observed 20th-century global mean surface warming only when both anthropogenic and natural forcings are included (Myhre et al. 2013). Compared to the pre-industrial levels, the concentrations of greenhouse gases such as CO_2, CH_4 and N_2O have increased significantly. The total radiative forcing (RF) of greenhouse gases is +2.83 (+2.54 to +3.12) Wm^{-2}. CO_2 is the most important climate forcing agent. It contributed an RF of about +1.68 ± 0.35 Wm^{-2} by infrared (IR) absorption (Figure 3). Additionally, the RF of CH_4 is +0.97 (+0.80 to +1.14) Wm^{-2}. The emission of CH_4 also leads to ozone production, stratospheric water vapour and generation of CO_2 and importantly, affects its own lifetime. Emissions of CO and non-methane volatile organic compounds (NMVOC) have only indirect effects on RF. Emissions of nitrogen oxides (NO_x) have indirect RF that lead to both of positive RF and negative RF (−0.15 (−0.34 to +0.02) Wm^{-2}). Although emissions of ammonia and sulphate have negative RF, black carbon (BC) has a positive RF due to aerosol–radiation interaction and BC on snow. Both BC and OM are emitted from various sources, such as biomass burning and fossil fuel. Although, aerosols have a very small net negative RF (~0.1 Wm^{-2}) by directly scattering and absorbing the solar radiation, the sign of the RF can change depending on the composition and source of aerosols (Figure 3). BC is considered to have a positive RF because its concentrations have increased and it has a strong light absorption from the ultra-violet (UV) to the near IR wavelength regions (Figure 3).

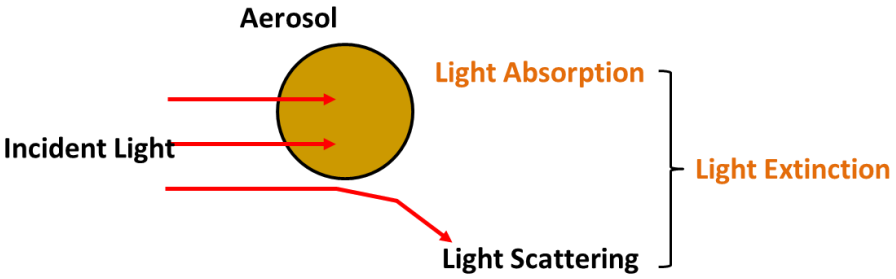

Figure 1. Interaction between light and aerosol particle; Sum of light absorption and light scattering are light extinction.

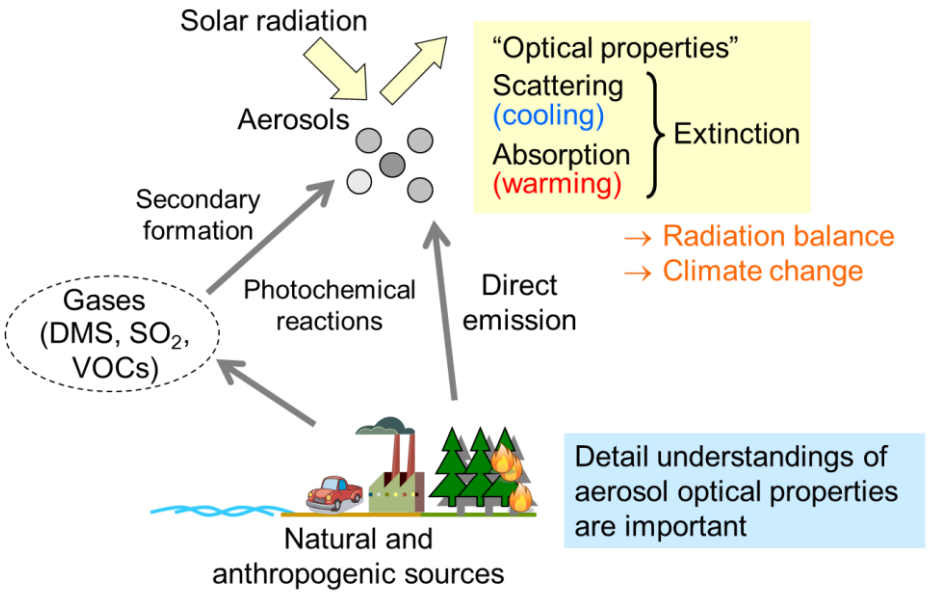

Figure 2. Schematic diagram of sources and optical properties of aerosol particles

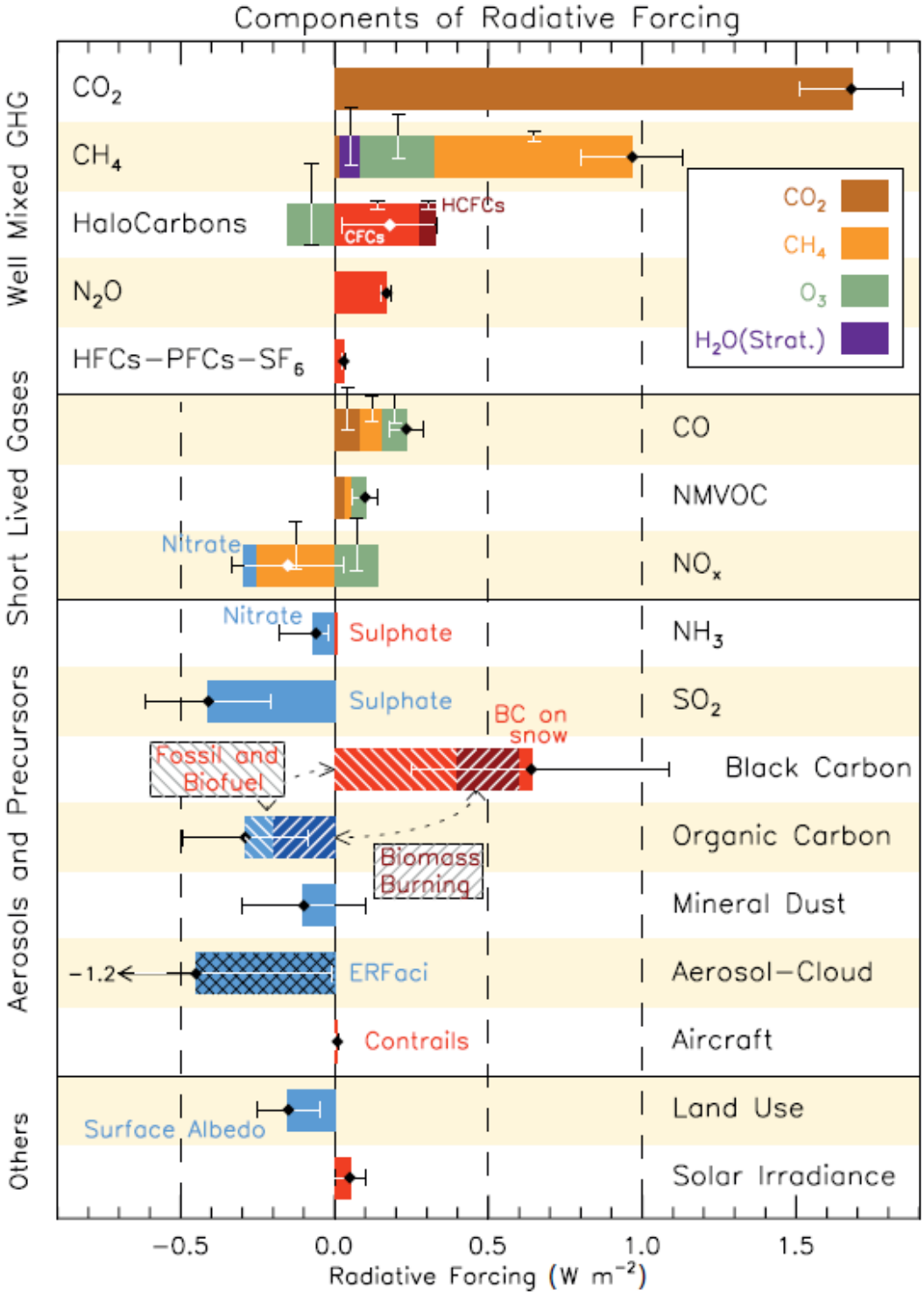

Figure 3. Radiative forcing of climate between 1750 and 2011 reported by IPCC AR5 (Myhre et al. 2013).

1.2. Sources and optical properties of carbonaceous aerosols

There are many emission sources and formation processes of carbonaceous aerosols involving BC and organic matter (OM). BC is considered to be generated from burning of fossil fuel or biomass, while OM can be generated from oxidation of VOCs in the atmosphere in addition to direct emission from fossil fuel such as propane and coal, as well as from burning of biomass such as wood, corn stem and rice straw (Figure 4).

BC is an important component of global warming in terms of direct RF (e.g. IPCC AR5). Control of atmospheric BC has been proposed as an important pathway to climate change mitigation. BC is defined operationally as carbonaceous material with a deep black appearance caused by a significant imaginary part of the RI. It roughly corresponds to elemental carbon (EC), which refers to non-volatile carbon below a certain temperature (typically 550°C) (Andreae and Gelencser 2006, Bond and Bergstrom 2006). Although the definitions of BC and EC are different, BC and EC are considered equivalent for the purpose of this work.

Recently, a class of OM called 'brown carbon' (BrC), which is defined operationally as light-absorbing carbonaceous material with a wavelength-dependent imaginary part of the RI was suggested to have the ability to absorb solar radiation, particularly at UV and shorter visible wavelengths (Figure 5). For example, the OM generated during photo-oxidation of aromatic hydrocarbons in the presence of NO_x has significant ^-values, typically at 300–500 nm (Zhong and Jang 2011, Liu et al. 2015). Nakayama et al. (2013) reported the RI-values at 405, 532 and 781nm for the secondary organic aerosols generated during photo-oxidation of toluene in the presence of NOx. They reported that the *k*-values at 405 nm were found to increase from 0.0018 to 0.0072 with increasing initial NOx concentration.

BrC has been considered to influence the radiation balance and photochemical reactions in the atmosphere (Andreae and Gelencser 2006, Moosmiiller et al. 2009, Nakayama et al. 2013, and references therein). It can be emitted from various sources (e.g. industry exhausts, diesel soot exhausts and biomass combustion), and BrCs from different sources undergo chemical processing and mix with each other. Different chemical processes influence chemical and optical properties of OM. However, only

~10% to 30% of the OM has been identified thus far. Most of the materials in atmospheric aerosols have not been characterized as individual compounds (Andreae 2009).

Aerosol can be classified in terms of thermochemical and optical properties (Figure 6). BC has the strongest light absorption and highest combustion temperature (lowest volatility). A fraction of OM has a characteristic absorption in the UV spectral range. These OMs have an important role in atmospheric photochemical processes, but they have almost no direct relevance to the RF determined by the absorption of visible radiation. BrC covers a broad range of moderately volatile organic compounds. It typically has a moderate amount of light absorption at short visible wavelengths (Andreae and Gelencser 2006). The difference in the wavelength dependence of BC and BrC has been used to quantify their contributions (e.g. Hadley et al. 2008).

As described previously, BC and OM play key roles in warming the atmosphere and have different physical and chemical properties. Recently, the enhancement of light absorption by BC internally mixed with OM (or other species such as sulphates and nitrates), which is referred to as the 'lensing effect' (Figure 7), is reported. Comparisons of enhancements of light absorption by coated BC with that by bare BC have been studied in several in-situ measurements. Nakayama et al. (2014) reported that enhancement of light absorption due to the lensing effect is different during August (~10% enhancement) and January (no enhancement) based on direct measurement of a three-wavelength photoacoustic soot spectrometer (PASS-3) at an urban site in Nagoya, Japan. The variations in the fraction of light absorbed (including contributions of the lensing effect) by OM were proposed to be caused by biomass burning. In other studies, the ratio of light absorption between ambient particles and bare BC has been reported to be ~1.0–1.43 in Toronto (Canada) (Knox et al. 2009, Chan et al. 2011, Healy et al. 2015) and 1.38 in Boulder (USA) (Lack et al. 2012).

Ueda et al. (2016) have reported that the average enhancement factor of BC light absorption due to coating was 1.22 at 781 nm, based on ambient observation using PASS-3 at an Asian outflow site in Noto Peninsula, Japan. They analysed samples using a transmission electron microscope (TEM) equipped with an energy dispersive X-ray analyser. The TEM results showed that coated BC particles with high enhancement ratios (>1.30 compared to uncoated BC) tended to be more spherical and thickly coated.

They suggested that the enhancement of light absorption is related to both the coating thickness (or amount of compound coated) and the spherical shape. The particle (mixing state) morphology can have the BC core either centrally or off-centrally located within the particle. The difference in morphology may contribute to the uncertainty of aerosol optical properties. To improve climate model performances, the knowledge of source and optical properties of BC and BrC are important.

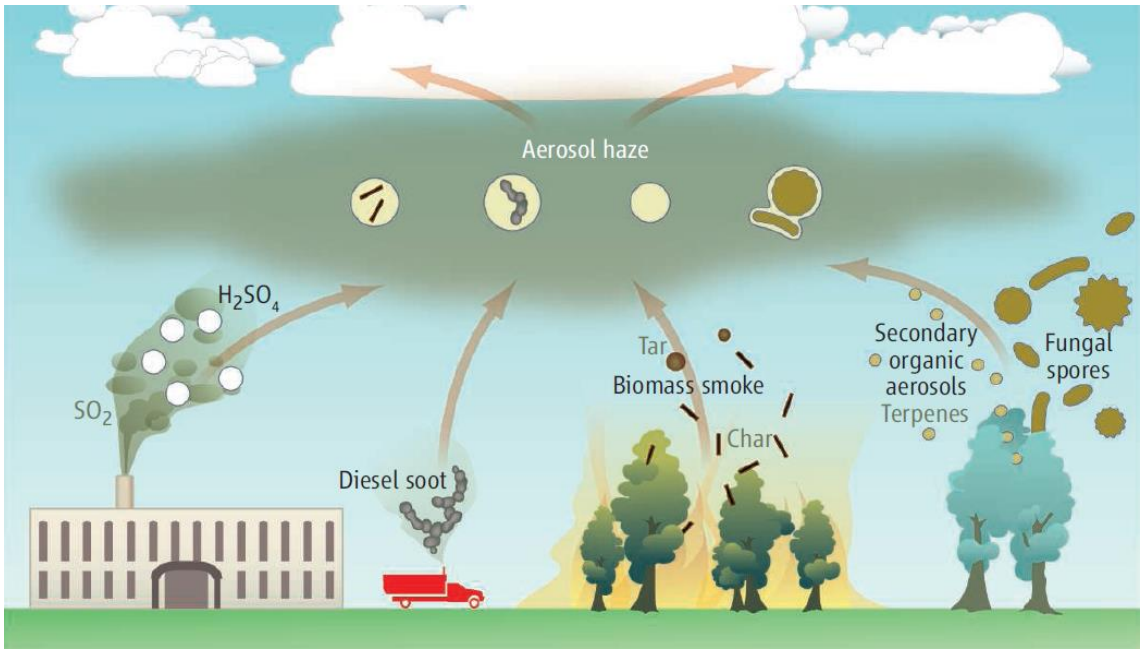

Figure 4. Emission and formation processes of carbonaceous aerosols (Andreae 2009).

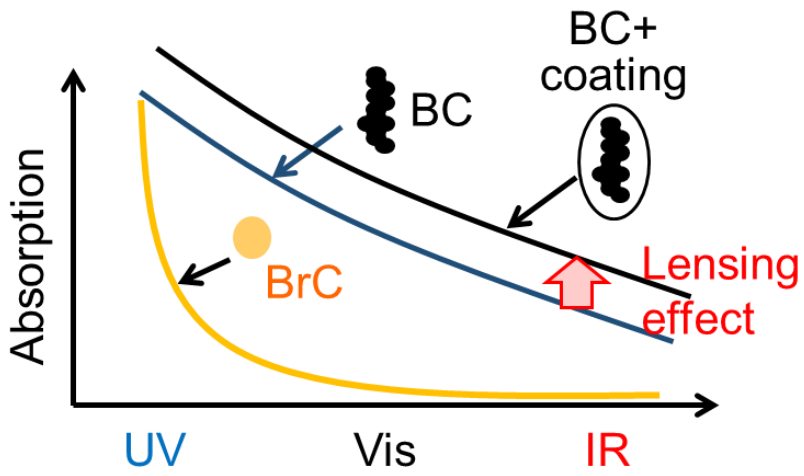

Figure 5. Schematic of wavelength dependence of light absorption of BC, coated BC, and brown carbon.

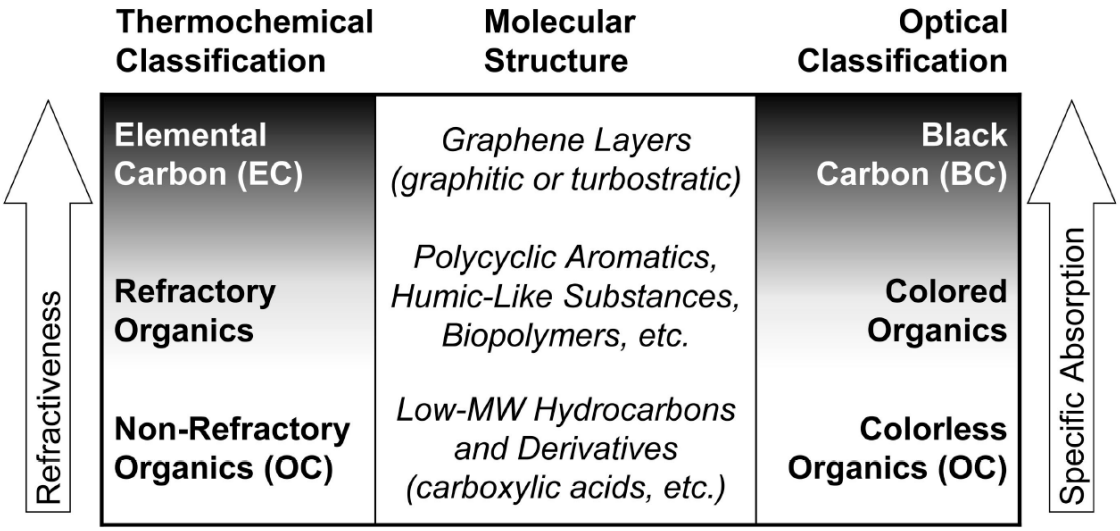

Figure 6. Thermochemical and optical classification of carbonaceous particles (Pöschl, 2003).

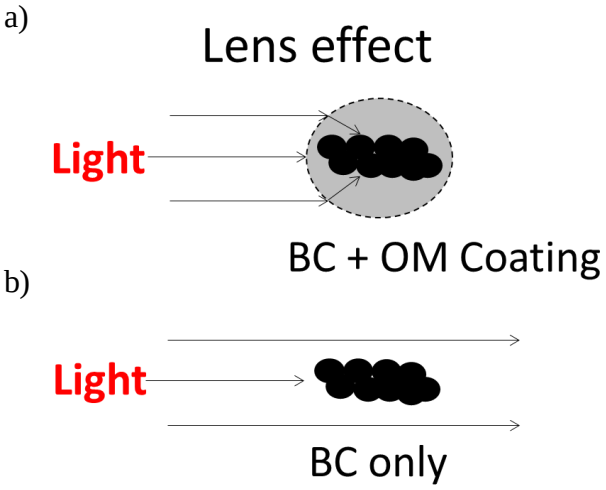

Figure 7. Schematic of the lensing effect. Light absorption of BC is considered to be enhanced by coating with other materials such as organic compounds

1.3. Conventional technique to measure light absorption of aerosols

Filter-based photometers such as Particle Soot Absorption Photometer (PSAP, Radiance Research) have been widely used to measure absorption coefficients. However, it is not easy to determine the contributions of the lensing effects and BrC on the basis of measurements using filter-based photometers. PSAP determines absorption coefficients from the temporal variation of light transmittance during the collection of aerosols on a filter (Figure 8). This method may lead to uncertainties owing to multiple scattering by the filter medium and coexisting particles and change in the physical shapes or chemical properties of aerosols on the filter. Lack et al. (2008) compared the absorption coefficients measured by PSAP and a photoacoustic spectrometer (PAS). A PAS can directly measure the absorption coefficients of aerosol particles suspended in air. They reported that PSAP overestimated absorption coefficients under high organic aerosol conditions (Figure 9). Nakayama et al. (2010) also reported that PSAP overestimated absorption coefficients for small particles due to the difference in the depth of particles trapped by the filter (Figure 10).

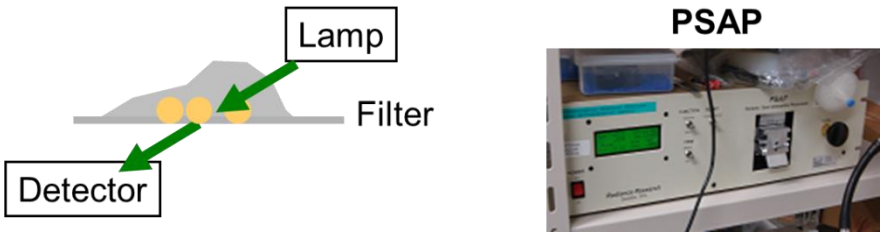

Figure 8. Schematic view and photograph of PSAP

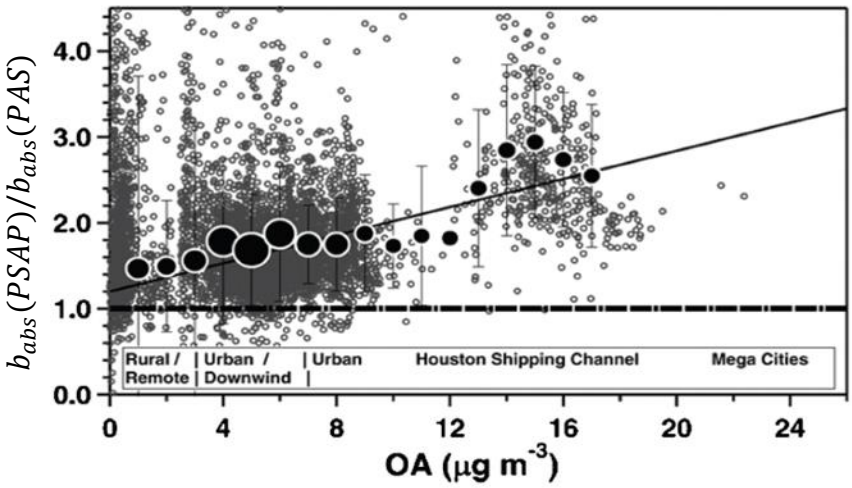

Figure 9. Dependence of ratio of absorption coefficients measured by PSAP to those measured by PAS on mass concentration of organic aerosols (Lack et al., 2008).

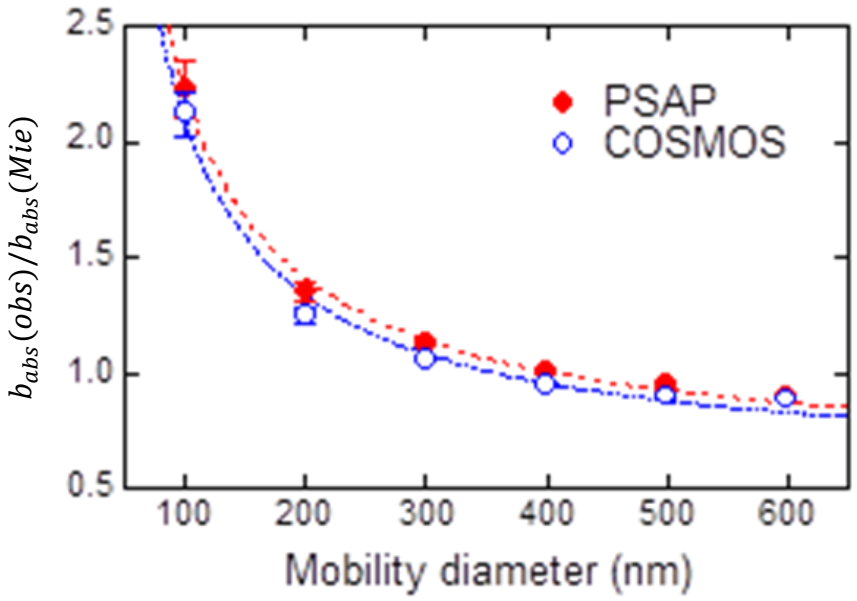

Figure 10. Dependence of ratio of absorption coefficients measured by PSAP to those calculated using Mie theory on mobility diameter of nigrosine particles (Nakayama et al., 2010).

1.4. BC and OM in diesel exhaust particles

Exhaust from motor vehicles such as diesel vehicles is one of the most important anthropogenic sources of carbonaceous particles in the atmosphere (e.g. Bond et al. 2013). Diesel exhaust particles (DEP) consist mostly of EC, OM and sulphur-containing compounds. EC is formed during combustion, and the relative contributions of EC in DEP vary from 5% to 90% depending on the engine type, after-treatment method and operating conditions (e.g. Moosmiiller et al. 2001, Maricq et al. 2007, Ronkko et al. 2007, Fushimi et al. 2011). A small fraction of the fuel and motor/lubricating oil is also exhausted directly without oxidation, depending on the different engine design or combustion conditions (Figure 11). The fraction associated with unburned fuel and lubricating oil is suggested to range from <10% to >90% (Sakurai et al. 2003). The OM in diesel exhaust contains chemicals such as aliphatic alkanes, cyclic alkanes, aromatic hydrocarbons and polycyclic aromatic hydrocarbons (PAHs) (Tobiias et al. 2001, Schauer et al. 1999, Zielinska et al. 2004, Huang et al. 2015). On the basis of gas chromatography analysis, Alam et al. (2016) have reported high carbon number ($>C_{15}$) n-alkanes, branched alkanes, alkyl cycloalkanes, alkyl benzenes, PAHs and other cyclic aromatics in diesel exhaust.

Because of the complex composition of primary vehicle exhaust particles, a full understanding of the optical properties of DEP is necessary. If a significant amount of OM exists internally mixed with BC in DEP, light absorption by BC may be enhanced. In addition, light-absorbing OM may be present in the DEP.

Recently, Adler et al. (2010) measured the optical properties of water-soluble material (WSM) and organic-soluble material (OSM) extracted from DEP collected on a filter and reported the imaginary part of the RI as 0.05 ± 0.02 (OSM) and 0.044 ± 0.001 (WSM) at 532 nm, and 0.11 ± 0.02 (OSM) and 0.07 ± 0.01 (WSM) at 355 nm. Using the RI values obtained, the influence of OM coating on the light absorption properties of BC was determined using the Rayleigh–Debye–Gans theory and the T-matrix method. The contributions of light-absorbing OM and the lensing effect on the light absorption properties of DEP depend on the mass ratio of BC to OM, size distribution and mixing state of DEP, and the RI of BC and OM, *i.e.* on the driving conditions. However, no experimental studies that focus on light-absorbing OM and the lensing effect using

real-time direct measurements of the wavelength dependence of optical properties have been reported.

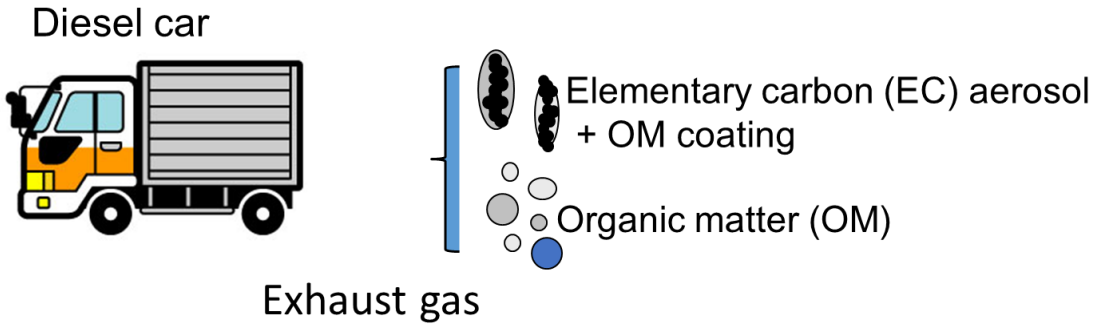

Figure 11. Carbonaceous particles containing in diesel exhaust

1.5. Purpose of this study

In this study, we measured wavelength-dependent absorption and scattering coefficients of DEP with and without passing the particles through a heater to investigate the contributions of light-absorbing OM and the lensing effect to the light absorption properties of DEP under a variety of driving conditions. To measure the optical properties of particles suspended in air directly in real time, we used a three-wavelength photoacoustic spectrometer (PASS-3, Droplet Measurement Technology).

Chapter 2

Experimental

2.1 Experimental setup

The test diesel engine vehicle used in the present study was the same as that used by Yamada et al. (2011), Yamamoto et al (2012), and Inomata et al. (2013), and was a light duty truck with a gross vehicle weight of 4485 kg and a 4.8 L engine equipped with a common rail injection system and diesel oxidation catalyst that complied with the emission regulations of Japan, 2003. Vehicle test runs were performed using a chassis dynamometer (Meidensha) in transient cycle (JE-05) or constant-speed (idling or driving at 70 km/h) driving modes (Figure. 12). The JE-05 mode, which is the Japanese approval test cycle for heavy-duty vehicles, is employed in the Japanese 2005 emission standards. For the JE-05 mode, the vehicle was warmed using a preconditioning cycle before the measurements were taken.

A schematic of the experimental setup is shown in Figure 13. The exhaust was diluted with air filtered using high efficiency particulate air and charcoal filters with a full flow constant volume sampler (CVS, Horiba, DLT-1860) at a flow rate of 40 m^3 min^{-1}. The exhaust gases and particles, which were sampled from the CVS, were additionally diluted with filtered air 6.4 and 3.3 times during the JE-05 and constant-speed modes, respectively. The diluted samples were passed through a heater and then introduced into the PASS-3. The heating system was used to separate BC and OM based on the difference in their thermal stabilities. The design of the heater was similar to that reported by Kondo et al. (2009) and consisted of a stainless steel tube and electronic jacket heaters. Most of the OM components should evaporate from particles in the heater maintained at 300-400°C (Kondo et al. 2009), while the BC components in the particle do not evaporate at these temperatures. Detailed characteristics of the heater are described in the Section 2.2. The temperature of the heated tube was maintained at 20, 47, or 300°C during the transient cycle mode and controlled between 20 and 400°C during the constant-speed mode, as listed in Table 1. Flow rate through the heater was

1.0 or 1.3 liter per minute (lpm) during the transient cycle and constant-speed modes, respectively, which correspond to a plug flow residence time of 2.9 and 2.3 sec (calculated at 20°C), respectively, in the heater. The heated tube temperature was monitored using a thermocouple. Particle transmission efficiency of the heater was tested in the laboratory using propane soot particles and found to be 0.80-0.98 depending on the heater temperature as described in the Section 2.2 and taken into account in the determinations of the optical properties and size distributions. Re-condensation of evaporated materials on the remaining particles after passing through the heater was negligible because of the smaller surface of those particles compared to that of the wall of the sampling line.

A PASS-3 instrument (Figure 14) was used to measure the absorption [$b_{abs}(\lambda)$] and scattering [$b_{sca}(\lambda)$] coefficients at 405, 532, and 781 nm. Information on the calibration procedures for the PASS-3 instrument is described in the Section 2.3. The b_{sca}(532 nm) data obtained using the PASS-3 were not used in this study because of the strong dependence of the calibration factors on particle size. Uncertainties associated with the calibration were estimated to be 4, 9, 11, 7, and 11% for b_{abs}(405 nm), b_{abs}(532 nm), b_{abs}(781 nm), b_{sca}(405 nm), and b_{sca}(781 nm), respectively. For background interpolation, measurements of filtered air were conducted using a particulate filter (Balston), typically for 2 min before and after running the JE-05 cycle during the transient cycle mode experiments, and every 6 min during the constant-speed mode experiments. Typical detection limits for the 2-sec (6 min) average data for b_{abs}(405 nm), b_{abs}(532 nm), b_{abs}(781 nm), b_{sca}(405 nm), and b_{sca}(781 nm) were estimated to be 11.2(3.5), 11.8(3.0), 6.4(1.4), 1.5(0.4), and 2.4(1.1) Mm^{-1}, respectively, by taking into account the standard deviation (2σ and drift of each signal during the filtered air measurements. Overall uncertainties for the PASS-3 data were estimated by accounting for uncertainties in the calibration factors and the background interpolations, and the detection limit values. Typical sampling flow rate of the PASS-3 was 1.0 lpm. The residence times from exhaust pipe to the PASS-3 were estimated to be 21 and 18 sec during the JE-05 and constant-speed modes, respectively. During constant-speed mode, size distributions of the DEP between 10-487 nm before and after heating were measured simultaneously every 3 min using two scanning mobility particle sizers

(SMPS, TSI, models 3936 and 3034, respectively), as shown in the upper chart of Figure 15. The particle size distribution during the JE-05 mode could not be determined because of the fast engine speed change compared to the scanning time intervals of the SMPS. Noted that the dilution ratio in the diluter was not taken into account in the reported $b_{abs}(\lambda)$and $b_{sca}(\lambda)$ values and size distributions.

The concentrations of gas phase nitrogen oxides (NO_x = NO + NO_2) and total hydrocarbons (THC) were also monitored using a conventional chemiluminescence instrument (Horiba, CLA-155) and a flame ionization detector (Horiba, FMA-125), respectively (Figure 13, gas analyzer). For the measurement of mass concentration, the DEP was also collected on a polytetrafluoroethylene (PTFE)-coated borosilicate glass fiber filter (Pallflex, TX40, 47 mm dia.) maintained at 52°C (Figure 13, filter sampler). The total sampling volumes during the JE-05 and constant-speed modes were approximately 1480 and 780 m^3, respectively. The mass concentration of total carbon (M_{TC}) was determined by weighing the filter samples before and after loading with particulates using a precision balance placed in a climate chamber at constant temperature and relative humidity (25°C and 40%, respectively). In addition, the mass concentration of OM (M_{OM}) was determined by re-weighing the filter samples after extracting the soluble organic fraction (SOF) *via* pressurized fluid extraction using an accelerated solvent extraction system (Dionex, ASE200), assuming that the contributions of inorganic compounds were negligible. This assumption is supported by the results of chemical composition measurements using an Aerodyne quadrupole-based aerosol mass spectrometer (Q-AMS). The mass concentration of EC (M_{EC}) was determined from the difference between the M_{TC} and $M_{OM.}$ The M_{EC}, M_{OM}, and M_{EC}/M_{TC} ratio values for each experimental run are listed in Table 1. Comparisons of the mass concentrations obtained by this solubility-based analysis with those obtained by the real-time measurement using the PASS-3 and Q-AMS are described in the section 2.4.

Five additional experimental runs to measure the chemical properties of the DEP emitted from the same vehicle running in the JE-05 mode were performed using an Aerodyne quadrupole-based aerosol mass spectrometer. Exhaust was introduced to the Q-AMS after dilution using the CVS. In the Q-AMS, particles collected through an

aerodynamic lens were heated at 600 K to evaporate the non-refractory materials, and the vaporized materials were then ionized via electron ionization and analyzed using a quadrupole mass spectrometer. Mass spectra were obtained every 6 sec and numerically analyzed using the AMS Analysis Toolkit ver. 1.41.

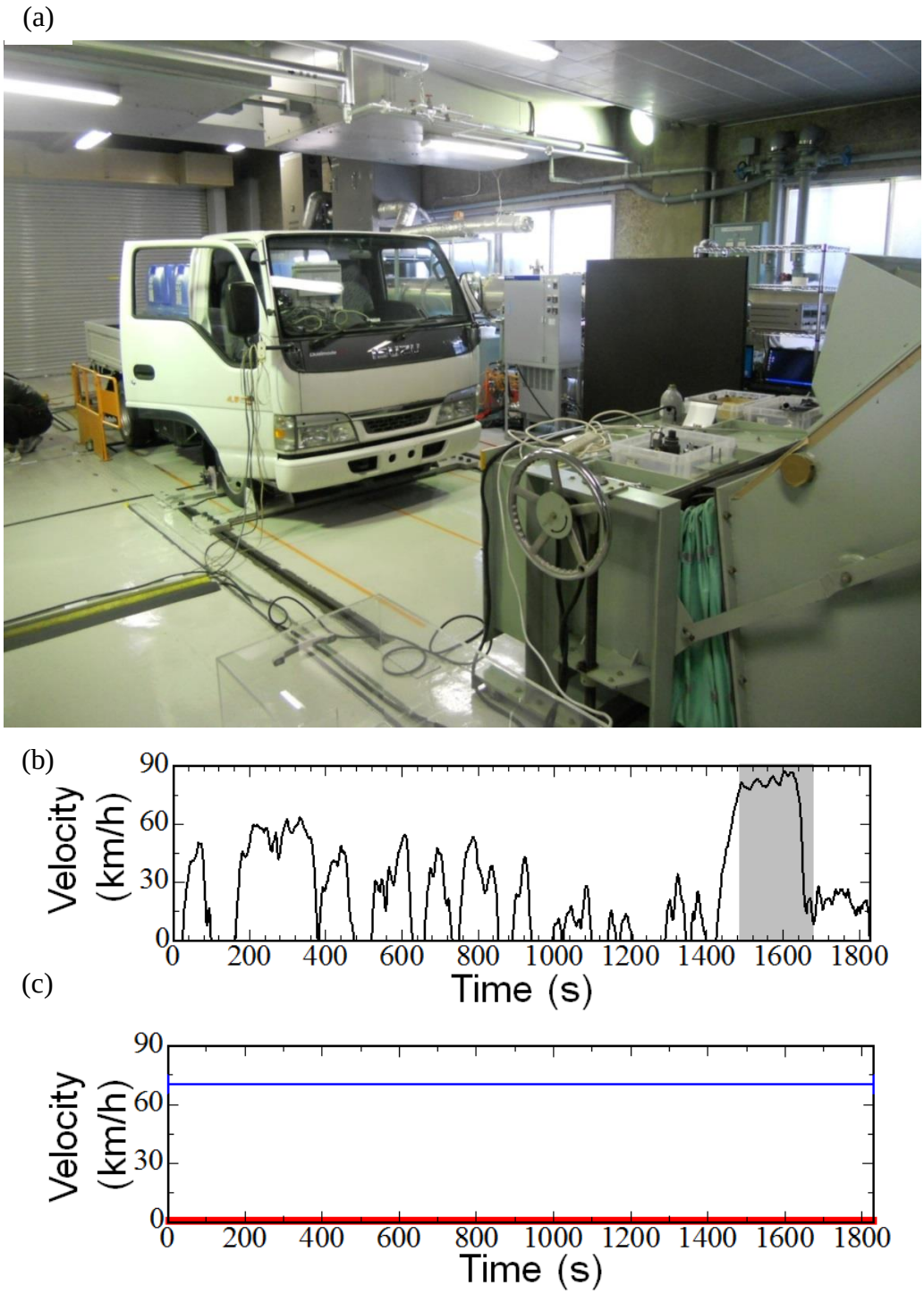

Figure 12. (a) A photograph of the light duty track running on the chassis dynamometer, (b) JE-05 mode (dash zone is high speed driving period), (c) Constant mode (driving in idling and 70km/h pattern)

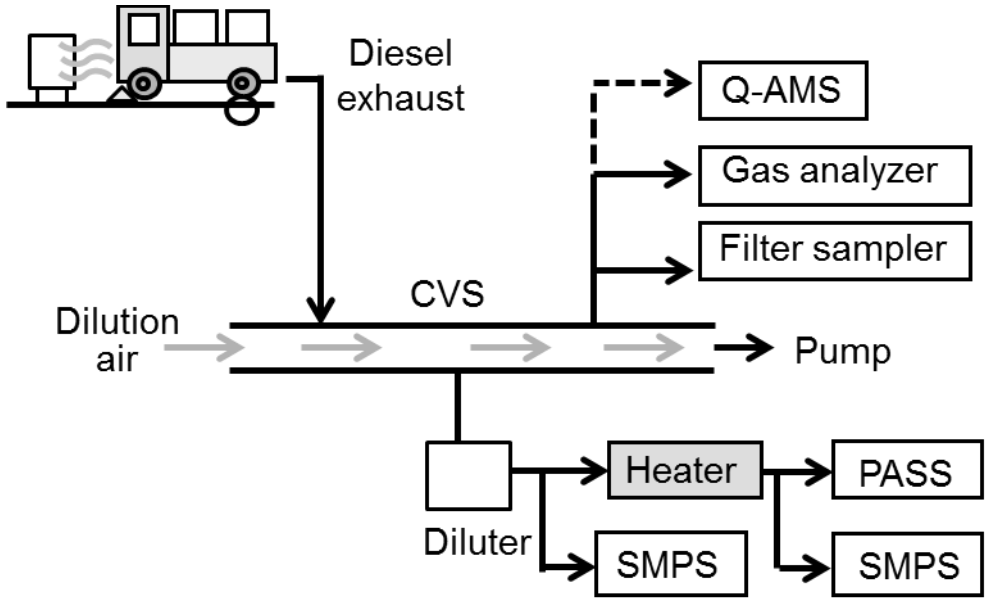

Figure 13. Schematic diagram of the experimental configuration. CVS: constant volume sampler; SMPS: scanning mobility particle sizer; PASS-3: three wavelength photoacoustic soot spectrometer; Q-AMS: quadrupole-based aerosol mass spectrometer. The SMPS was used only during the constant-speed modes.

Table 1. Experimental conditions, EC and OM mass concentrations, and EC/TC mass fraction ratio.

No.	Driving mode [a)]	Heater Temp. (°C)	M_{EC} [b)] (mg/m^3)	M_{OM} [b)] (mg/m^3)	M_{EC}/M_{TC} [b)]
1	JE-05 mode	20	0.28	0.19	0.60
2	JE-05 mode	47	0.27	0.18	0.61
3	JE-05 mode	300	0.26	0.17	0.61
4	Constant-speed mode (Idling)	20-400	0.10 ± 0.02	0.06 ± 0.01	0.63 ± 0.09
5	Constant-speed mode (70 km/h)	20-400	0.31 ± 0.03	0.15 ± 0.02	0.67 ± 0.05

a) All experiments were conducted under hot-start driving condition.

b) Average mass concentrations of EC and OM, and EC/TC mass fraction. Particles were collected on a filter, maintained at 52°C. Mass concentrations were measured after diluting with CVS (Figure. 13).

a)

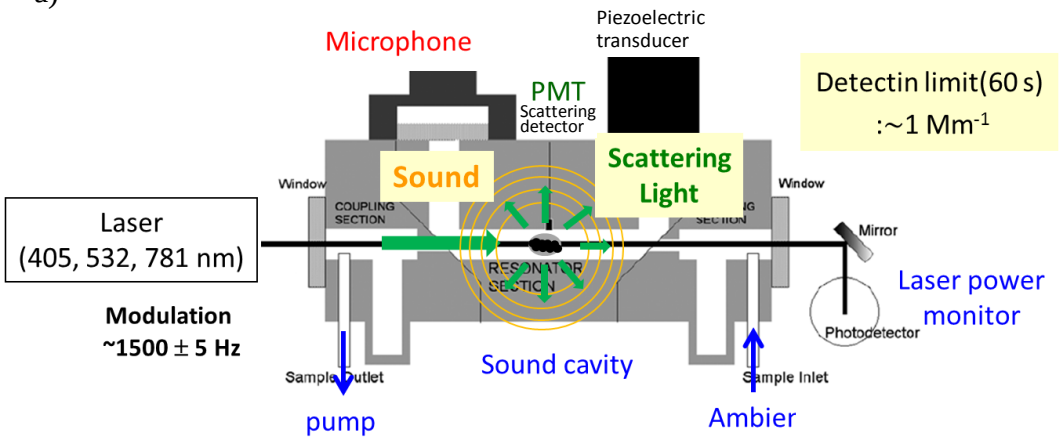

b)

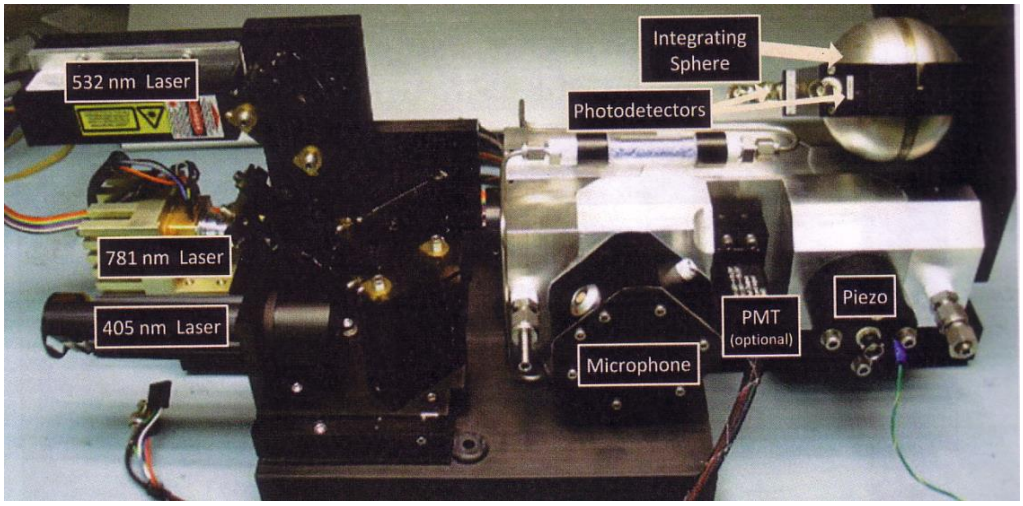

Figure 14. a) Schematic (modified from Lewise et al. 2008) and b) photograph (PASS-3 operator manual, Droplet Measurement Technology, 2011) of the PASS-3

2.2 Characteristics of the heater

The heater (Figure 15) consisted of a stainless steel tube (outer and inner diameters: 12.7 and 10.2 mm, respectively; length: 600 mm) and electronic jacket heaters (Heater Engineer, P-series) and was used to determine the temperature dependence of the optical properties of diesel exhaust particles. Temperature of the heated tube was maintained at 20, 47, or 300°C during the transient cycle mode and controlled between 20 and 400°C during the constant-speed modes using a home-made temperature controller. Flow rate through the heater was 1.0 or 1.3 lpm for experiments using the transient cycle and constant-speed modes, respectively, which correspond to plug flow residence times of 2.9 and 2.3 sec (calculated at 20°C), respectively, in the heater. Temperature of the heated tube was monitored using thermocouple "A" (type K) placed 45 cm from the inlet of the heated tube, as shown in Figure 16. Temperature profiles inside the heated tube were measured by sliding a second thermocouple "B" (type K) from the outlet side when the tube temperature was 47 and 300°C; also shown in Figure 16. The centerline temperatures were nearly constant near the middle of the tube. The temperature monitored using thermocouple "A" was referred to as the "heater temperature" throughout the study.

Particle loss in the heater was examined by simultaneously measuring the size distribution of propane soot particles before and after they passed through the heater using two different scanning mobility particle sizers (SMPS, TSI, model 3936). The propane soot particles were passed through another heater maintained at 400°C before obtaining the measurements to avoid any possible contributions from volatile components. The sample and sheath flows for the SMPS were maintained at 0.3 and 3.0 lpm, respectively, and size distributions between 14 and 750 nm were measured every 5 min. The slight difference in the sensitivity of the two SMPS (typically <5%) was taken into account by simultaneously measuring the size distribution of propane soot particles without passing through the heater before and after the experiments. Figure 17 shows mobility size dependence of the soot particle transmission efficiencies through the heater at temperatures of 20, 100, 200, and 300°C and a flow rate of 1.3 lpm. Transmission efficiencies were nearly constant for mobility diameters greater than 60

nm. Temperature and flow rate dependence of the transmission efficiencies for each experimental condition in the present study were then calculated from the average of the transmission efficiencies greater than 60 nm, and are shown in Figure 18. Transmission efficiency at 200°C, 0.87 ± 0.03, was consistent with that for a heater (0.88) reported by Cappa et al. (2012, supplemental material) and was slightly greater than those for thermodenuders with charcoal denuders reported by Cappa et al. (2012, supplemental material) and Huffman et al. (2008).

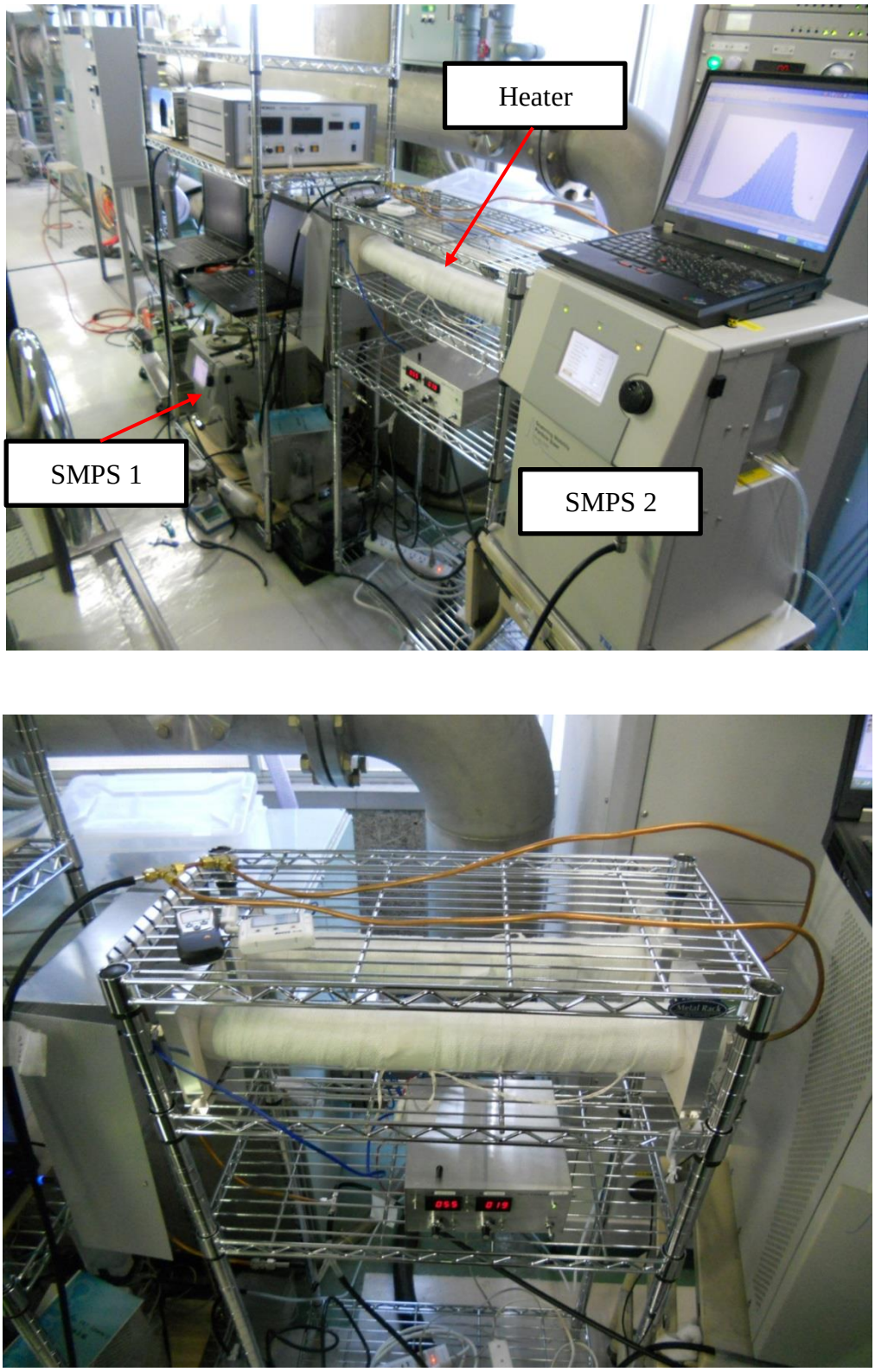

Figure 15. Photographs of the heaters used in this experiment

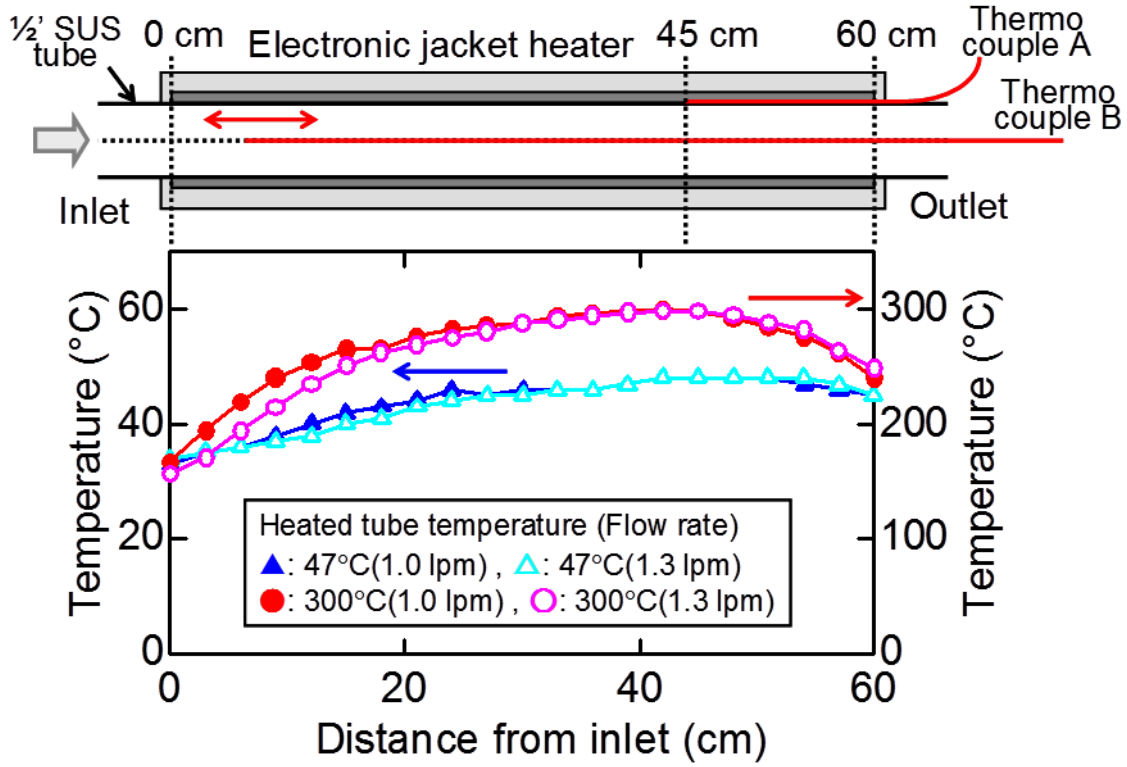

Figure 16. Schematic of the heater along with temperature profiles along the centerline of the heated tube measured using thermocouple "B" when tube temperature was controlled at 47 and 300°C using thermocouple "A" at sample gas flow rates of 1.0 and 1.3 lpm.

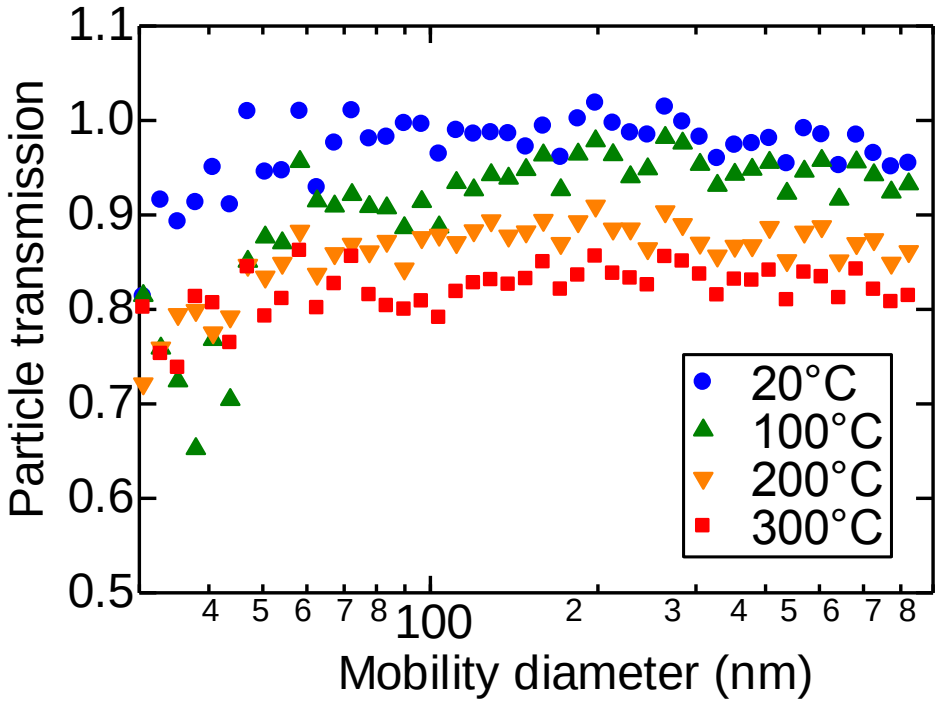

Figure 17. Mobility size dependence of soot particle transmission efficiency through the heater at the temperatures of 20, 100, 200, and 300°C and a flow rate of 1.3 lpm.

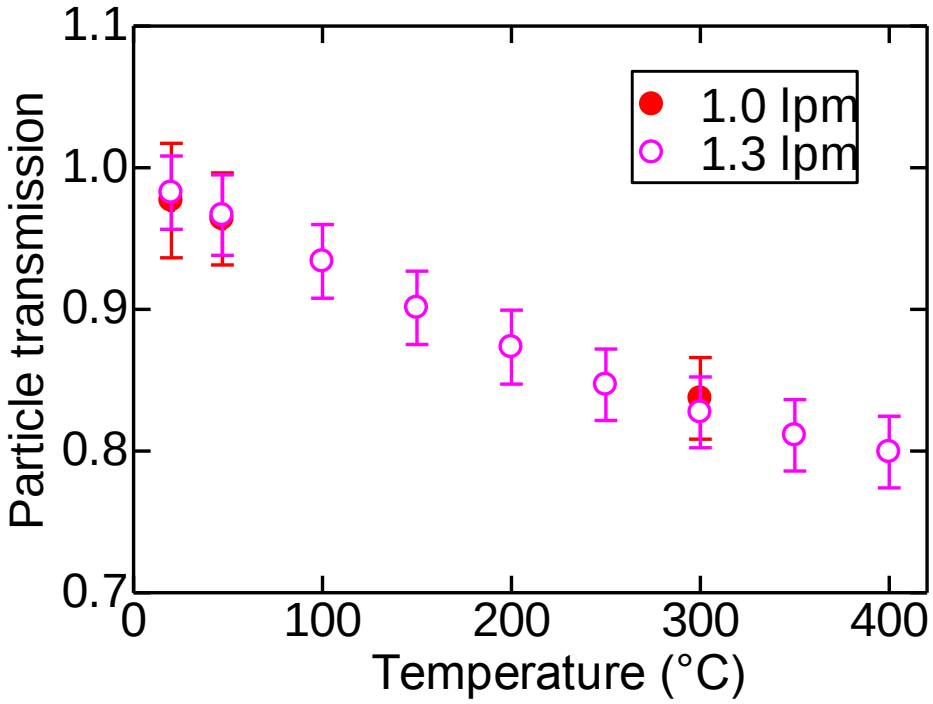

Figure 18. Temperature dependence of average transmission efficiency of soot particles with a diameter >60 nm from 20-400°C at flow rates of 1.0 and 1.3 lpm.

2.3 Calibration of the PASS-3

The PASS-3 measurements of light absorption and scattering of particles are based on photoacoustic spectroscopy and reciprocal nephelometry. Detailed analyses of performance of the PASS-3 are described elsewhere (Nakayama et al. 2015), and only a brief description of the calibration procedures used for the present study is provided here.

Calibration for scattering measurements was conducted using monodisperse polystyrene latex (PSL) particles with diameters of 203, 299, or 400 nm (Duke Scientific), generated by an atomizer. The particles were dried using a diffusion dryer with silica gel and then were passed through a differential mobility analyzer (DMA) (TSI, model 3081) and an aerosol particle mass analyzer (APM) (Kanomax, model 3601). The calibration factors for scattering measurements were determined by comparing observed scattering coefficients using the PASS-3 with those calculated based on Mie theory using particle diameter, particle number density measured by a condensation particle counter (CPC) (TSI, model 3772), and reported refractive index values (Matheson and Saundersson 1952, Nikolov and Ivanov 2000, Pettersson et al. 2004, Baynard et al. 2007, AboRiziq et al. 2007, Lang-Yona et al. 2009, and Washenfelder et al. 2013). Truncation angles estimated from the particle size dependence of the calibration factor (Nakayama et al. 2015), and uncertainty in the determination of the calibration factors were used to estimate the overall uncertainty of the correction factors for scattering as 7, 27, and 11%, at λ = 405, 532, and 781 nm, respectively, when measuring strongly light-absorbing particles with volume-based geometric mean diameter of less than 500 nm. The large uncertainty at 532 nm was due mainly to the strong particle size dependence of the calibration factors.

Calibration for absorption measurements was conducted using high concentrations of poly-dispersed propane soot particles. The soot particles were introduced into the PASS-3 after passing through diffusion dryers with silica gel and through a heater maintained at 300°C to remove volatile materials such as organic compounds. Calibration factors for absorption measurements were determined by comparing the observed absorption coefficients with those obtained from subtraction of the corrected $b_{sca}(\lambda)$ from the $b_{ext}(\lambda)$ using the Beer-Lambert law based on change in

light intensity passing through the acoustic cell in the presence and absence of particles. Overall uncertainties in the correction factors for absorption were estimated to be 4, 9, and 11% at λ = 405, 532, and 781 nm, respectively, by considering uncertainties in the comparison, in determination of $b_{ext}(\lambda)$, and in the correction factors for scattering measurements. The AAE values between 405-781, 405-532, and 532-781 nm for the propane soot particles, which were calculated by taking the calibration factors into account, on averaged 1.02, 1.26, and 0.86, respectively. Calibration factors at 405, 532 and 781 nm varied 4, 9, and 11%, respectively, resulting in an expectation that the average AAE values between 405-781, 405-532, and 532-781 nm would vary between 0.87-1.21, 0.94-1.61, and 0.59-1.17, respectively. Observed differences in the AAE values for the three selected wavelength pairs were smaller than variations of those values expected from the estimated errors in the calibration factors. Results of observed AAE values close to 1.0 and smaller variations in AAE compared to those expected from the estimated errors in the calibration factors suggest that the calibration factors and their uncertainties are reasonable.

To check the temporal variation in the sensitivity (calibration factors) of scattering and absorption measurements at 405 and 532 nm, Rayleigh scattering of CO_2 and light absorption of high concentration of NO_2 (up to 201 ppm in air) were used. No significant change in the sensitivity of scattering and absorption measurements at 405 and 532 nm was found for any of the experiments.

The ratio of the absorption coefficients measured for different heater temperatures were used for estimating the lensing effects and contributions of light absorption by OM in the present study. The absolute values of the calibration factors do not change the conclusions, although unexpected systematic uncertainties in the calibration factors cannot be ruled out.

2.4 Comparison of filter based analysis with real-time measurements

The M_{EC} and M_{OM} values based on a solubility-based analysis of filter samples were compared with the average mass concentrations of optically equivalent BC (M_{EBC}) and organics (M_{org}) calculated from real-time measurement data obtained using PASS-3 and Q-AMS.

The M_{EBC} values in the CVS were estimated from the average b_{abs}(532 nm) data measured at a heater temperature at 300°C using the mass absorption cross section (MAC_{BC}) of 7.75 ± 1.24 m^2g^{-1} calculated from the value at 550 nm for fresh soot particles reported by Bond and Bergstrom (2006) assuming an AAE of 1.0 and taking the dilution ratio into account. The M_{EBC} values obtained during JE-05 mode, idling, and constant-speed driving at 70 km/h were estimated to be 0.17 ± 0.05, 0.09 ± 0.02, and 0.19 ± 0.03 mg/m^3, respectively, where the uncertainties were related to the measurement of b_{abs}(532 nm) and the MAC_{BC}. The M_{EBC} values during JE-05 mode and constant-speed driving at 70 km/h were 35 and 39% less than M_{EC}, while those during idling agreed well with M_{EC} (Table 1). The dependence of the MAC_{BC} value on the particle size, as well as the uncertainties in dilution ratio, may contribute to these differences.

Because the real-time measurements of organics using Q-AMS were conducted as separate experiments, the average of the M_{org} values for the JE-05 mode measured using Q-AMS for five experimental runs were used for the comparison. The average M_{org} value was calculated to be 0.082 ± 0.014 mg/m^3. This small M_{org} value compared to the M_{OM} (~0.18 mg/m^3) may be due partly to uncertainties in collection efficiency (CE) of the Q-AMS. Although a CE of 0.5, commonly used for atmospheric aerosol studies, was used in the present study, smaller CE values also have been reported, especially under dry conditions (Middlebrook et al. 2012). Recent laboratory studies reported CE values ranging from less than 0.15 to unity for secondary organic aerosols generated in a chamber (Docherty et al. 2013). Because no validation of the CE value was conducted in the present study, the absolute values of M_{org} were not used for the discussion.

Chapter 3

Results and Discussion

3.1 Aerosol optical properties in transient cycle mode (JE-05)

3.1.1 Absorption and scattering coefficients

For the transient cycle mode, three experimental runs were conducted using different heater temperatures (20, 47, and 300°C). Figure 19 shows temporal variation in the $b_{abs}(\lambda)$ and $b_{sca}(\lambda)$ values measured using the PASS-3 at a heater temperature of 20°C during the JE-05 driving cycle. Temporal variations in vehicle speed and mixing ratio of THC ([THC]) and NO_x ([NO_x]) are also shown in Figure 19. The time delay between emission from the exhaust pipe to measurement in each instrument was taken into consideration in the analyses. The values for b_{abs} and $b_{sca,}$ as well as those for [THC] and [NO_x], increased during acceleration and were greatest during the high-speed driving period between 1480 and 1650 sec, corresponding to driving on a highway. In particular, a large enhancement of b_{sca} was observed just after completing a hard acceleration to high-speed (~1500 sec) and just after initiating deceleration from high-speed (~1630 sec). Enhancement should actually occur within a shorter timescale than that observed because of the smoothing effect upon passage through the dilution tunnel and secondary dilution system. Average values for $b_{abs}(\lambda)$ and $b_{sca}(\lambda)$ during the high-speed driving period and other periods are listed in Table 2. Ratios of the average of b_{abs} at 405, 532, and 781 nm during the high-speed driving period to corresponding values during the other periods were 2.2, 1.8, and 1.7, respectively, while similar ratios of the average values of b_{sca} at 405 and 781 nm were 7.4 and 3.3, respectively. The greater enhancement of b_{sca} compared to that of b_{abs} during the high speed driving period suggests a larger increase in the emission of OM with less (or no) light-absorbing ability compared to that of strongly light-absorbing BC during this period, although a possible contributions of the change in particle size cannot be ruled out. Temporal variation in the organics, shown in Figure 19 (e), supported the large enhancement of

OM emissions during the high-speed driving period, particularly when a large enhancement of b_{sca} was observed (~1500 and ~1630 sec). The change in combustion conditions may enhance OM emission. The mass concentrations of sulfate, nitrate, ammonium, and chloride measured using the Q-AMS remained less than 10 μ g/m^3 throughout the JE-05 mode.

Figure 20 shows temporal variation in $b_{abs}(\lambda)$ and $b_{sca}(\lambda)$ measured at inlet heater temperatures of 47 and 300°C, which were conducted as separated experimental runs with that conducted at inlet heater temperatures of 20°C. Because the mass loading of DEP varied slightly in each experimental run, the values for $b_{abs}(\lambda)$ and $b_{sca}(\lambda)$ at 47 and 300°C were corrected to those at 20°C by multiplying $M_{TC}(20°C)/M_{TC}$(47 or 300°C), where $M_{TC}(T)$ is mass concentration of total carbon during the measurement with inlet heater temperatures of T. A portion of OM should evaporate during filter sampling because the sampler was maintained at 52°C. However, the uncertainties in the correction to b_{abs} and b_{sca} should be small (<5%) even if half of the OM is assumed to evaporate during filter sampling, because no significant difference in M_{EC}/M_{TC} ratios was observed for the three experiments (Table 1) and the run-to-run variations in average mass concentrations of organics in the JE-05 mode measured by the Q-AMS were relatively small (16%, 1 σ value for five experimental runs).

The average values for b_{sca} at 405 and 781 nm decreased dramatically to 15 and 51%, respectively, of the b_{sca} values obtained at 20°C upon heating the DEP to 300°C during the high-speed driving period (Table 2). In contrast, these values decreased to 84 and 75%, respectively, of the b_{sca} values at 20°C, during the other periods. These results suggest that the emission of OM, which evaporated at temperatures lower than 300°C, increased during the high-speed driving period. In addition, the values for b_{sca} at 405 and 781 nm during the high-speed driving period decreased on average to 66 and 83% of the b_{sca} value at 20°C upon heating to 47°C. A portion of the OM was thought to evaporate at temperatures lower than 47°C. Furthermore, b_{abs} values at 405 and 532 nm decreased upon heating to 300°C during the high-speed driving period, but did not decrease significantly during the other periods, and no significant decrease in the value of b_{abs} at 781 nm was observed for either period.

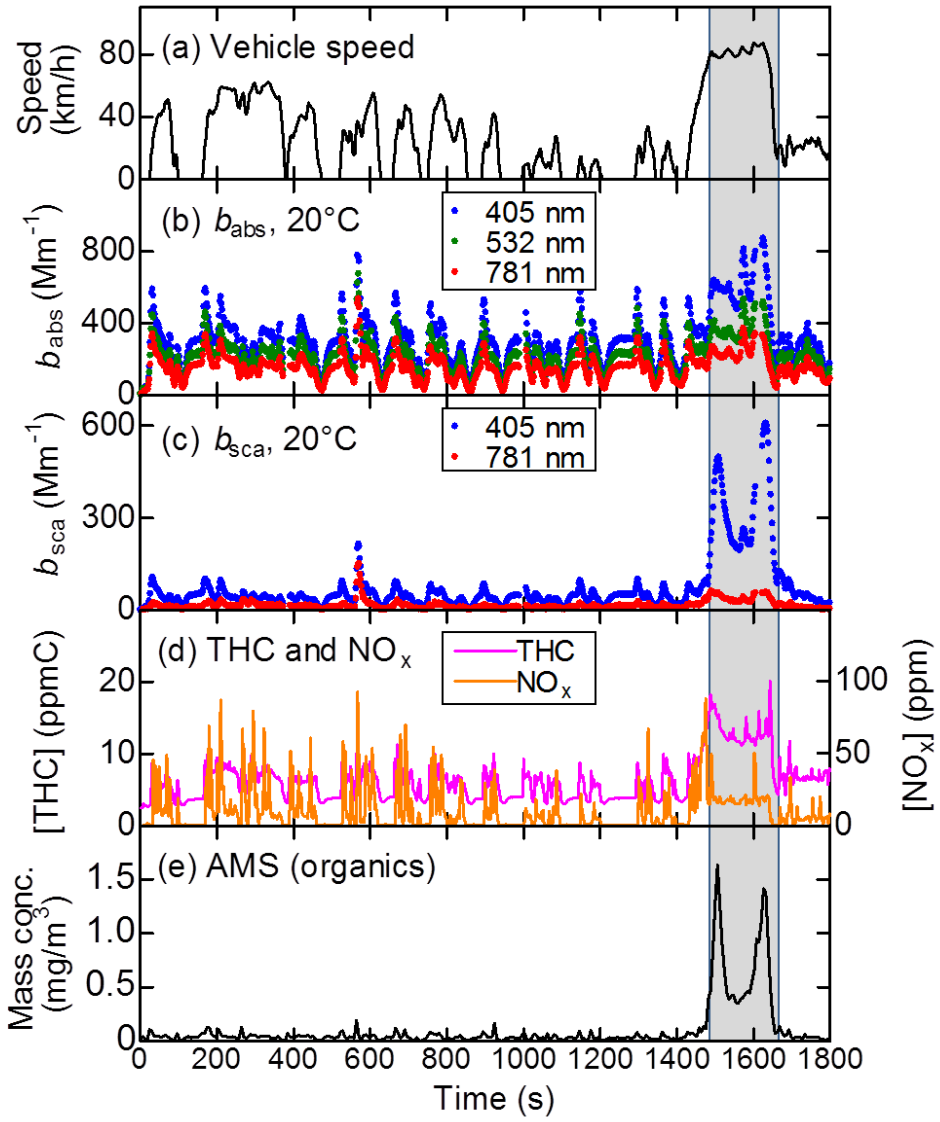

Figure 19. Temporal variations in (a) vehicle speed, (b) absorption, and (c) scattering coefficients, and (d) mixing ratios of THC and NO_x measured during JE-05 mode with a heater temperature of 20°C. Panel (e) shows the temporal variation in mass concentrations of the organics measured using Q-AMS during a separate experimental run (collection efficiency is assumed to be 0.5). The time delay between emission and measurement for each instrument was corrected. The $b_{abs}(\lambda)$ and $b_{sca}(\lambda)$ values were measured after diluting with CVS and the other diluter, while the [THC], [NO_x], and AMS (organics) values were measured after diluting with the CVS (see Figure. 13). The dilution factors were not taken into accounts for these values. The period between 1480 and 1650 sec was defined as the high-speed driving period.

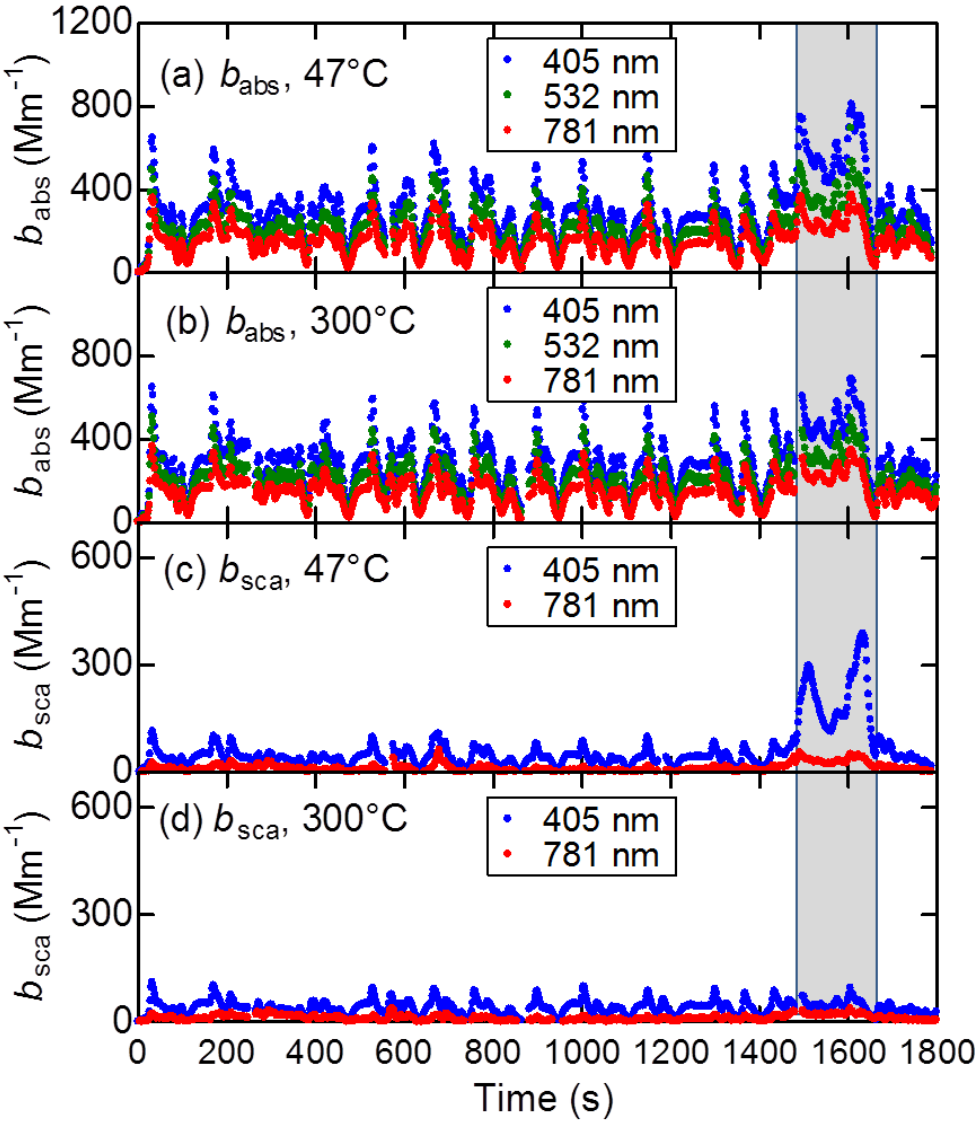

Figure 20. Temporal variations in (a and b) absorption and (c and d) scattering coefficients measured in JE-05 mode with heater temperatures of 47 and 300°C.

Table 2. Average (± 1 σ) for absorption (b_{abs}) and scattering (b_{sca}) coefficients, single scattering albedo (SSA), and absorption Ångström exponent (AAE) during the high-speed driving period and other periods in JE-05 mode.

	High speed driving period [a]			Other periods [a]		
	20°C [b]	47°C [b]	300°C [b]	20°C [b]	47°C [b]	300°C [b]
b_{abs}(405 nm) (Mm^{-1})	596 ± 117	572 ± 121	476 ± 97	274 ± 120	274 ± 117	271 ± 115
b_{abs}(532 nm) (Mm^{-1})	362 ± 77	369 ± 90	333 ± 72	202 ± 93	201 ± 91	198 ± 89
b_{abs}(781 nm) (Mm^{-1})	238 ± 53	246 ± 61	236 ± 52	142 ± 71	140 ± 67	139 ± 66
b_{sca}(405 nm) (Mm^{-1})	325 ± 134	216 ± 82	49 ± 14	44 ± 27	41 ± 22	37 ± 20
b_{sca}(781 nm) (Mm^{-1})	41 ± 11	34 ± 8	21 ± 4	12 ± 12	8 ± 8	9 ± 7
SSA(405 nm) [c]	0.34 ± 0.08	0.27 ± 0.06	0.09 ± 0.01	0.13 ± 0.04	0.13 ± 0.03	0.12 ± 0.02
SSA(781 nm) [c]	0.15 ± 0.04	0.12 ± 0.02	0.08 ± 0.01	0.08 ± 0.04	0.06 ± 0.03	0.07 ± 0.03
AAE(405 nm/532 nm) [c]	1.84 ± 0.32	1.64 ± 0.30	1.33 ± 0.15	1.16 ± 0.27	1.16 ± 0.24	1.16 ± 0.28
AAE(532 nm/781 nm) [c]	1.09 ± 0.12	1.06 ± 0.12	0.89 ± 0.12	0.97 ± 0.22	0.93 ± 0.19	0.91 ± 0.21

a) High-speed driving period; 1480-1650 sec, other periods; 0-1480 and 1650-1830 sec.

b) Heater temperature

c) Only b_{abs} and b_{sca} data greater than the detection limits were used for calculating SSA and AAE.

3.1.2 Single scattering albedo and absorption Ångström exponent

Figure 21 shows the temporal variation in the single scattering albedo (SSA) calculated using the obtained $b_{abs}(\lambda)$ and $b_{sca}(\lambda)$ values and the following equation:

$$SSA(\lambda) = b_{sca}(\lambda) / [b_{abs}(\lambda) + b_{sca}(\lambda)]. \quad (1)$$

The average SSA values during the high-speed driving period and the other periods are listed in Table 2. An increase in the value of SSA was observed during high-speed driving at heater temperatures of 20 and 47°C. The average $\pm 1\ \sigma$ SSA values at 405 and 781 nm measured at 20°C during the high-speed driving period were 0.34 ± 0.08 and 0.15 ± 0.04, respectively. In contrast, relatively small and constant SSA values (0.09-0.13 and 0.06-0.08 at 405 and 781 nm, respectively) were observed during the other periods at 20 and 47°C, and for all of the periods at 300°C. These results suggest that the OM was emitted mainly during the high speed driving period, and that most of the OM evaporated at 300°C. The smaller SSA value at 781 nm compared to that at 405 nm may be explained by the greater wavelength dependence of the scattering coefficients compared to that of absorption coefficients for sufficiently small particles.

Figure 22 shows the temporal variation in absorption Ångström exponent (AAE) calculated using the $b_{abs}(\lambda)$ and $b_{sca}(\lambda)$ values and the following equation:

$$AAE(\lambda_1/\lambda_2) = -\ln(b_{abs}(\lambda_1)/b_{abs}(\lambda_2))/\ln(\lambda_1/\lambda_2). \quad (2)$$

The average AAE values during the high-speed driving period and other periods are listed in Table 2. The AAE(532 nm/781 nm) values remained fairly constant and close to unity (on average 0.89-1.09) during all of the periods for all temperatures. In addition, the AAE(405 nm/532 nm) values also were close to unity (on average 1.16) during the other periods for all temperatures studied. These values were consistent with the literature values for BC particles without a coating (Bond and Bergstrom, 2006). In contrast, a significant increase in the AAE(405 nm/532 nm) value was observed at 20 and 47°C during the high-speed driving period, particularly when a large enhancement in b_{sca} was observed (~1500 and ~1630 sec). Interestingly, the average AAE(405 nm/532 nm) value during the high-speed driving period at 20°C (1.84 ± 0.32) was slightly larger than that at 47°C (1.64 ± 0.30). Recently, Lack and Cappa (2010) reported that the AAE value for BC typically does not exceed 1.6, even when coated

with non-light-absorbing materials. Therefore, the present results suggest that the light-absorbing OM contributes significantly to the observed aerosol absorption at 405 nm during the high-speed driving period at 20 and 47°C.

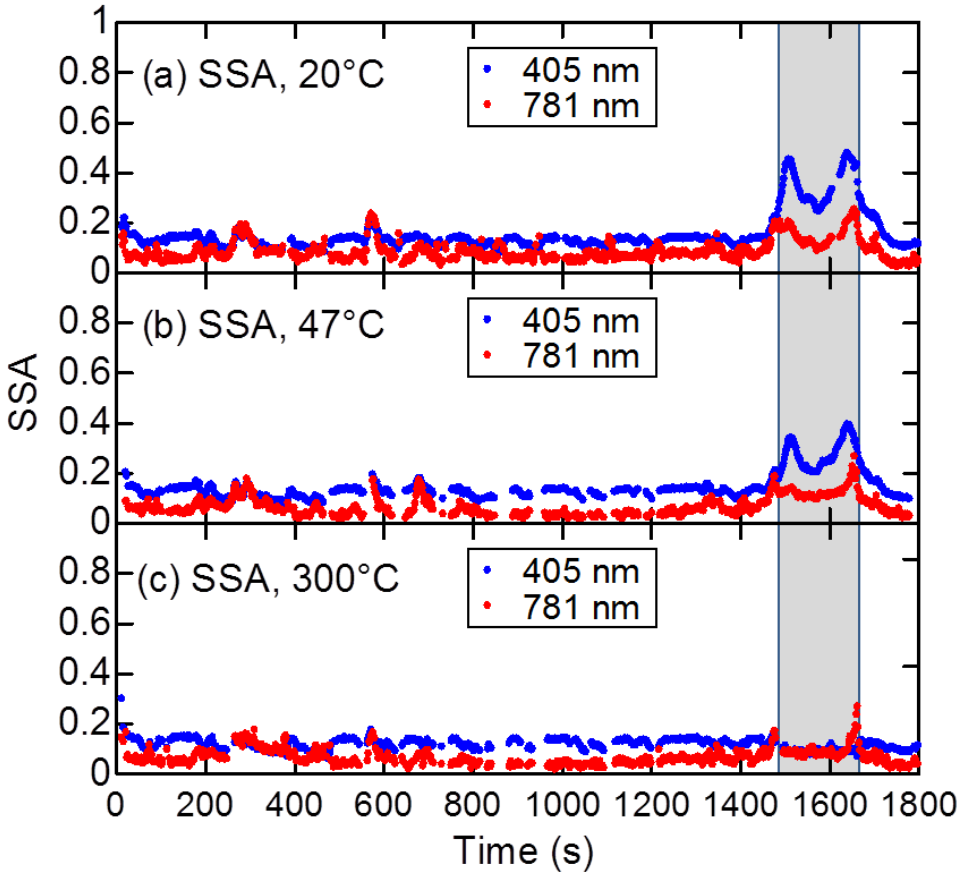

Figure 21. Temporal variations in SSA during JE-05 mode with heater temperatures of (a) 20, (b) 47, and (c) 300°C, calculated using eq. (1).

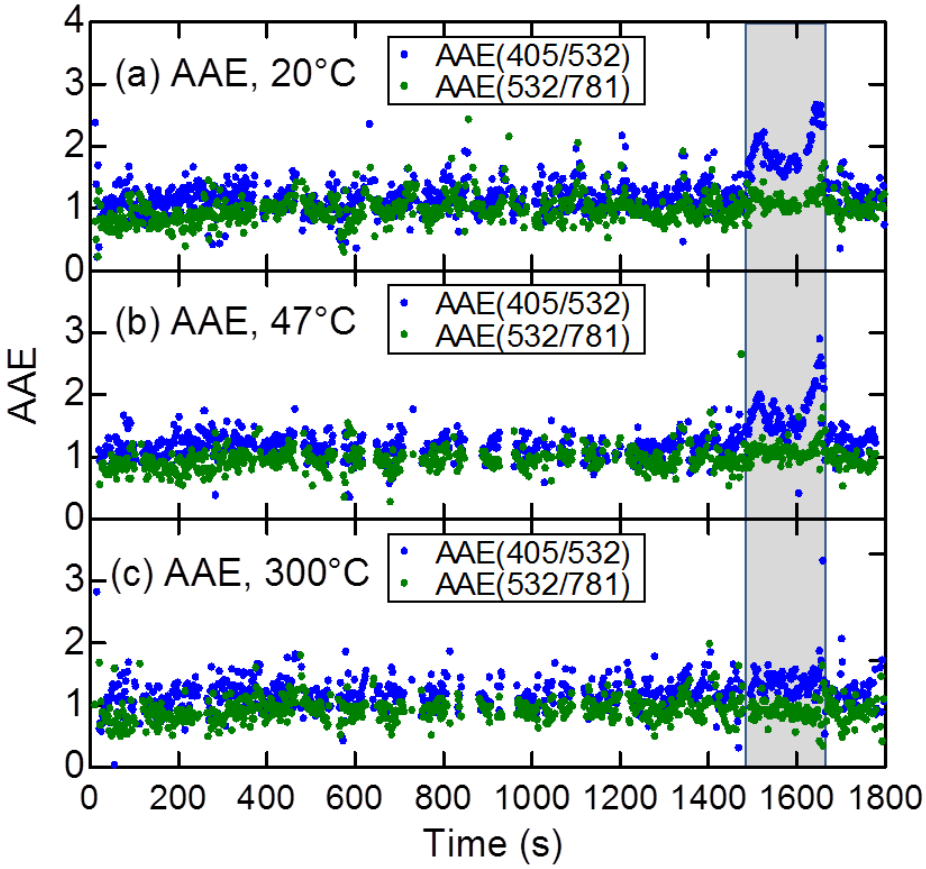

Figure 22. Temporal variations in AAE during JE-05 mode with heater temperatures of (a) 20, (b) 47, and (c) 300°C, calculated using eq. (2).

3.1.3 Contributions of the lensing effect and light-absorbing OM

Contributions of the lensing effect and the light-absorbing OM were determined by calculating the absorption enhancement factors ($E_{abs}(\lambda, T)$, T = 300°C) using the following equation:

$$E_{abs}(\lambda,T) = b_{abs}(\lambda, 20°C) / b_{abs}(\lambda,T) \quad (3)$$

Averages of the values during the high-speed driving period and other periods are listed in Table 3.

The coating thickness and light absorption of the OM that evaporated at temperatures below 300°C, as well as the shape of the BC core, contributed to value of $E_{abs}(\lambda, 300°C)$. When light absorption by the OM is negligible and the shape of the BC core does not change with heating up to 300°C, $E_{abs}(\lambda, 300°C)$ represents the enhancement of the light absorption due to coating formation. At 781 nm, light absorption by the OM is negligible. Although the mass concentration of the organics was enhanced during the high-speed driving period, the E_{abs}(781nm, 300°C) values during this period (1.06 ± 0.10) were consistent with those during the other periods (1.04 ± 0.24). This result implies that the enhancement of light absorption by coating BC with OM (lensing effect) was minimal for exhaust particles during the high-speed driving period. It is likely that the OM components externally mix with the BC, or that the BC components are located at the edges of particles, even if the OM and BC components are internally mixed in the same particles.

In contrast, $E_{abs}(\lambda, 300°C)$ values at 405 and 532 nm (1.34 ± 0.15 and 1.14 ± 0.10, respectively) were greater during the high-speed driving period, while the $E_{abs}(\lambda, 300°C)$ values at 405 and 532 nm (1.05 ± 0.23, 1.05 ± 0.22, respectively) during the other periods were similar to those at 781 nm. These results, along with the AAE values near unity during the other periods, can be explained by assuming that the contribution to light absorption by the OM at 405 and 532 nm is insignificant during the other periods, due to the small fraction of OM (Figure 19(e)).

The approximate ratios of the effective absorption coefficients for OM [$b_{abs,OM}(\lambda)$] to the observed absorption coefficient [$b_{abs}(\lambda)$] at λ = 405 and 532 nm were then calculated using procedure similar to that described in Cappa et al. (2012):

$$b_{abs,OM}(\lambda) / b_{abs}(\lambda) = [E_{abs}(\lambda, 300°C) - E_{abs}(781\ nm, 300°C)] / E_{abs}(\lambda, 300°C) \quad (4)$$

where it is assumed that value of E_{abs}(781 nm, 300°C) represents enhancement of light absorption of BC due to coating and that this factor is the same as that at 405 and 532 nm. Temporal variation in the $b_{abs,OM}(\lambda)/b_{abs}(\lambda)$ values at 405 and 532 nm is shown in Figure 23, and the average values during the high-speed driving period and other periods are listed in Table 3. Using these results, the contributions of light absorption by the OM, which evaporated at temperatures below 300°C, to the total aerosol light absorption at 405 and 532 nm, were estimated to be 20 ± 7 and 7 ± 6% during the high-speed driving period, and 0 ± 8 and 1 ± 9% during the other periods, respectively. Changes in the mixing state and particle shape during heating may also have influenced these estimates.

Recently, nitro-aromatic compounds, such as nitrophenols, in organic aerosols have been proposed as a source of light absorption at UV and shorter visible wavelengths (Jacobson 1999, Nakayama et al. 2010, 2013, Zhong and Jang 2011, Zhang et al. 2011, 2013 Zhong et al. 2012, Mohr et al. 2013). Inomata et al. (2013) measured gas-phase volatile organic compounds emitted from the same vehicle used in the present study during the JE-05 mode using a proton-transfer mass spectrometer (PTR-MS) and detected nitro-aromatics, including nitrophenols. They also detected nitrophenols in particles *via* liquid chromatography-mass spectrometry (LC-MS) analyses of the DEP collected on a filter (Inomata et al. 2013). Therefore, nitro-aromatics are plausible candidates as the source of light absorption observed during the high-speed driving period, although the contributions of other compounds cannot be ruled out.

Table 3. Average ($\pm$ 1 σ) of absorption enhancement factors and ratio of effective absorption coefficient for OM to observed absorption coefficient during the high-speed driving period and other periods in JE-05 mode.

	High-speed driving period [a)]	Other periods [a)]
E_{abs}(405 nm, 300°C) [b)]	1.34 ± 0.15	1.05 ± 0.23
E_{abs}(532 nm, 300°C) [b)]	1.14 ± 0.10	1.05 ± 0.22
E_{abs}(781 nm, 300°C) [b)]	1.06 ± 0.10	1.04 ± 0.24
$b_{abs,OM}$(405 nm)/ b_{abs}(405 nm) [b)]	0.20 ± 0.08	0.00 ± 0.08
$b_{abs,OM}$(532 nm)/ b_{abs}(532 nm) [b)]	0.07 ± 0.06	0.01 ± 0.09

a) High-speed driving period; 1480-1650 sec, other periods; 0-1480 and 1650-1830 sec.

b) Only b_{abs} and b_{sca} data greater than the detection limits were used for the calculations.

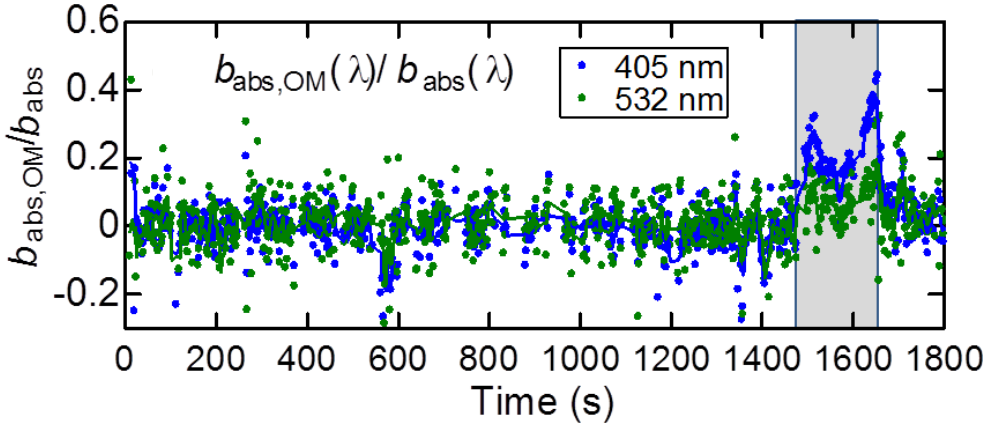

Figure 23. Temporal variations in ratios of effective absorption coefficient for OM to observed absorption coefficient at 405 and 532 nm during the JE-05 mode. Solid lines show the 5-point moving average.

3.2 Aerosol optical properties constant-speed driving mode

3.2.1 Absorption and scattering coefficients

For the constant-speed driving mode, temperature dependence of the optical properties and the size distributions of the DEP were measured under two different driving conditions: idling and driving at 70 km/h. The temperature of the heater was varied stepwise from 20 to 400°C, and the optical properties and size distributions were measured for 12 - 24 min at each temperature. Because mass loading of the DEP varied slightly during the temperature-dependence measurements, $b_{abs}(\lambda)$ and $b_{sca}(\lambda)$ values measured at temperatures greater than 47° C were corrected to those at 20°C using the change in total particle volume, which was calculated from the size distribution determined using other SMPS without heating. The corrected average $b_{abs}(\lambda)$ and $b_{sca}(\lambda)$ values obtained at inlet heater temperatures of 20, 47, and 300°C are listed in Table 4.

The b_{abs} values at 405, 532, and 781 nm measured at a heater temperature of 20°C while idling were approximately 50% of those obtained while driving at 70 km/h. However, the $b_{sca}(\lambda)$ values at 405 and 781 nm were greater while idling than those obtained while driving at 70 km/h (Table 4). These results can be explained by the emission of larger particles during idling, as indicated in the particle size distributions presented in Figure 24, and by the greater particle size dependence of the scattering efficiency compared to that of the absorption efficiency when the particle size is sufficiently smaller than the wavelength (Bohren and Hoffman 1983).

Taking into account the difference in the dilution ratio, b_{abs} values at 405, 532, and 781 nm at 20°C during the constant-speed driving at 70 km/h were 53-68% of those for the high-speed driving period in JE-05 mode, while the b_{sca} values at 405 and 781 nm were 11-15% of those for the high-speed driving period in JE-05 mode. The large difference in the b_{sca} values for the constant-speed driving and JE-05 modes may be due to the lower emission of OM during constant-speed driving, because the mass concentration of OM during high-speed driving (~80 km/h) in JE-05 mode should be several times greater than the average values during the JE-05 mode (Table 1) and greater than those during constant-speed driving mode (70 km/h). This difference in OM emissions is likely caused by the difference in acceleration pattern rather than the

difference in driving speed.

As shown in Table 4, b_{sca}(405 nm) values decreased on average to 72 and 79% of the b_{sca} values at 20°C during idling and driving at 70 km/h, respectively, upon heating the DEP to 300°C. The small decrease in b_{sca}(405 nm) values compared to those during the high-speed driving period in JE-05 mode can be explained by the smaller emission of OM during constant-speed driving. Furthermore, no significant decrease in b_{abs} was observed at any wavelength upon heating to 300°C during both idling and driving at 70 km/h.

Table 4. Average (±1 σ) for absorption (b_{abs}) and scattering (b_{sca}) coefficients at inlet heater temperatures of 20, 47 and 300°C during the constant-speed driving modes.

	Idling			Driving at 70 km/h		
	20°C [a)]	47°C [a)]	300°C [a)]	20°C [a)]	47°C [a)]	300°C [a)]
b_{abs}(405 nm) (Mm^{-1})	284 ± 8	292 ± 8	291 ± 9	612 ± 18	617 ± 17	597 ± 16
b_{abs}(532 nm) (Mm^{-1})	212 ± 6	218 ± 6	225 ± 8	438 ± 12	444 ± 13	434 ± 13
b_{abs}(781 nm) (Mm^{-1})	152 ± 4	157 ± 4	162 ± 5	314 ± 8	319 ± 9	313 ± 8
b_{sca}(405 nm) (Mm^{-1})	84 ± 2	87 ± 2	61 ± 2	69 ± 3	66 ± 2	55 ± 2
b_{sca}(781 nm) (Mm^{-1})	16 ± 1	16 ± 2	12 ± 1	12 ± 1	12 ± 1	11 ± 2

a) Heater temperature

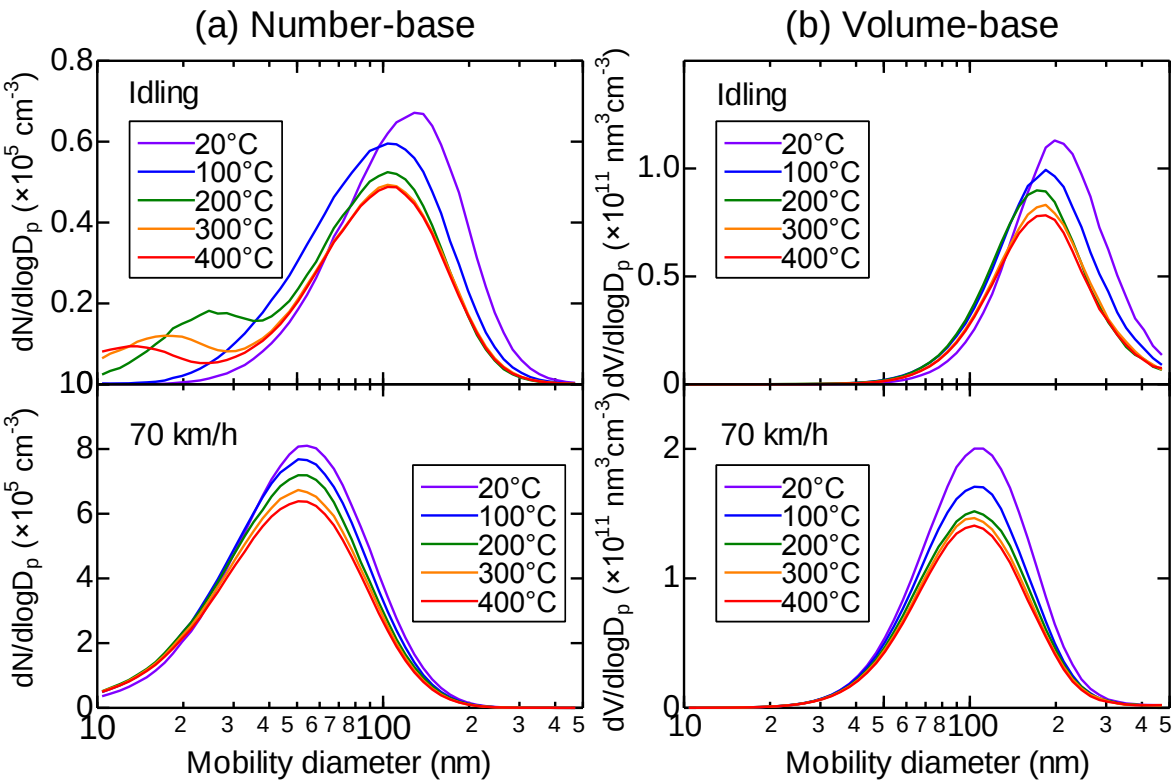

Figure 24. (a) Number- and (b) volume-weighted size distributions of DEP measured at heater temperatures of 20, 100, 200, 300, and 400°C, during constant-speed driving modes: (upper panels) idling and (lower panels) driving at 70 km/h. Because the mass loading of DEP varied slightly during the temperature-dependence measurements, size distributions were corrected using the change in the total particle number and volume concentrations, measured using other SMPS without heating the DEP. The SMPS measurements were performed after diluting with CVS and other diluter (Fig. 13). Dilution factors were not taken into account in the concentration values.

3.2.2 Single scattering albedo and absorption Ångström exponent

The dependence of SSA and AAE on the inlet heater temperature when idling and driving at 70 km/h is shown in Figure 25. Larger SSA values were observed while idling than while driving at 70 km/h, and the SSA values at 405 nm were greater than those at 781 nm. These results may be due to the differences in particle size and the wavelength dependence of absorption and scattering efficiency (*i.e.*, the scattering efficiency is greater at shorter wavelengths and for larger particles emitted during idling). The ranges of SSA values obtained during the constant-speed mode and other periods in JE-05 mode, 0.08 - 0.22 at 405 nm and 0.03 - 0.11 at 781 nm, are consistent with the literature values of 0.18, 0.16, and 0.13 at 450, 550, and 700 nm, respectively, for fresh diesel soot particles (Schnaiter et al. 2005).

While both idling and while driving at 70 km/h, no significant temperature dependence of AAE(405 nm/532 nm) and AAE(532 nm/781 nm) values was observed between 20 and 400°C within the uncertainties, as shown in Figure 25. The temperature-independence of the AAE(405 nm/532 nm) that are close to unity during the constant-driving mode implies that the contribution of light absorption by the OM, which evaporated below 400°C, was small.

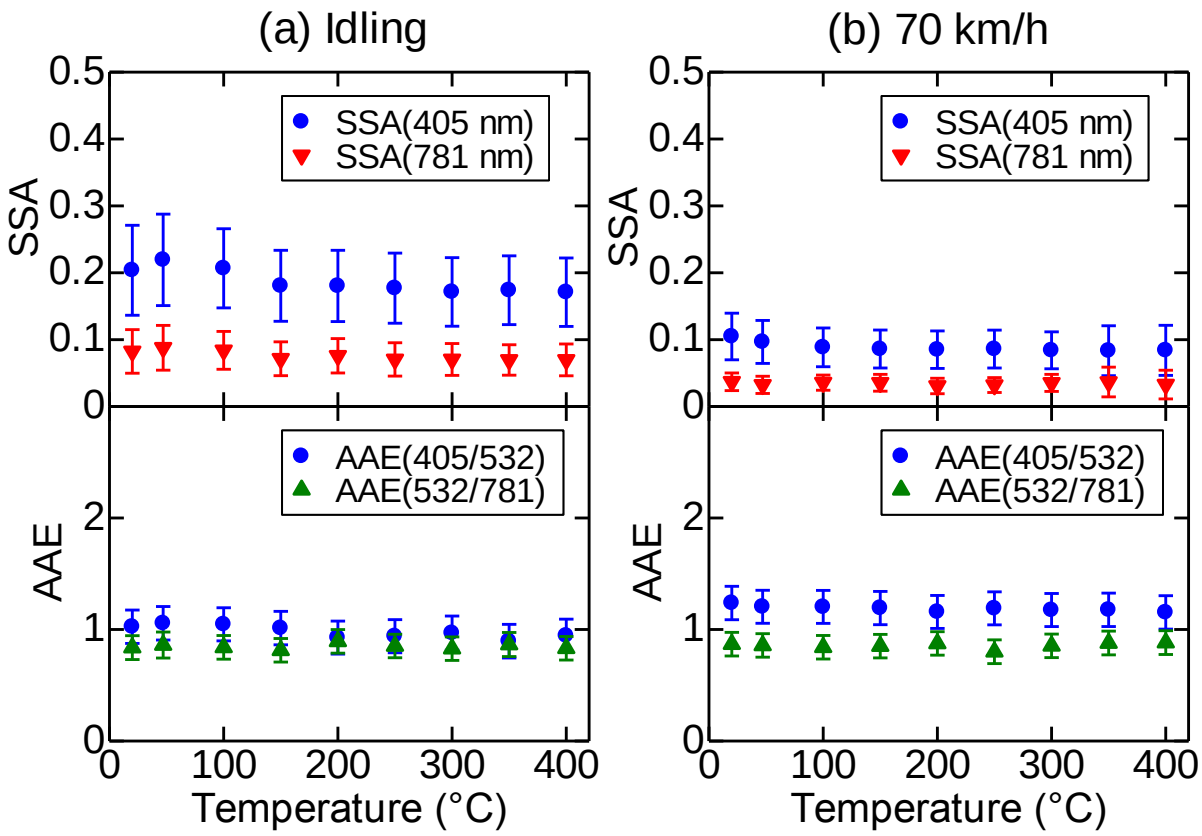

Figure 25. Heater temperature dependence of (upper panels) SSA and (lower panels) AAE during constant-speed driving modes: (a) idling and (b) driving at 70 km/h.

3.2.3 Contributions of lensing effect and light-absorbing OM

The dependence of enhancement factor $E_{abs}(\lambda, T)$ values on heater temperature while idling and while driving at 70 km/h, calculated using eq. (3), is shown in Figure 26 (upper panels). The E_{abs} values at 405, 532, and 781 nm were consistent within the uncertainties, and no heater temperature dependence of E_{abs} was observed when either idling or driving at 70 km/h.

The number and volume fraction remaining (NFR and VFR) for the DEP after heating were calculated using the temperature dependence of the size distributions and are shown in Figure 26 (lower panels). The VFR for particles emitted during idling and driving at 70 km/h when heated to 400°C were 0.75 ± 0.05 and 0.71 ± 0.06, respectively. These values are consistent with the M_{EC}/M_{TC} ratios (0.63 ± 0.09 and 0.67 ± 0.05, respectively (Table 1)), although differences in the density and shape of the BC (or EC) and OM-containing particles as well as evaporation of OM during filter sampling also contribute to the difference.

Assuming internally mixing of all of the OM with BC, the potential for enhancement of light absorption by BC coated with co-emitted OM was estimated using the core-shell Mie theory (Bohren and Huffman, 1983). The absorption enhancement factor ($E_{abs,cal}$) at each heater temperature (T) was calculated using the following equation:

$$E_{abs,cal}(\lambda, T) = b_{abs,core\text{-}shell}(\lambda, 20°C) / b_{abs,core\text{-}shell}(\lambda, T), \qquad (5)$$

where $b_{abs,core\text{-}shell}(\lambda, 20°C)$ and $b_{abs,core\text{-}shell}(\lambda, T)$ are the absorption coefficients at a wavelength λ for heater temperatures of 20°C and T, respectively, calculated using the core-shell Mie theory. In this calculation, the size distribution of the DEP measured at a heater temperature of 400°C was used as the size distribution for the BC core. The coating thickness was estimated from the difference in total particle volume between each temperature (20-350°C) and 400°C, assuming that all of the non-refractory materials evaporated between each temperature and 400°C coated the BC and that the core-shell ratio did not depend on particle size. The complex refractive index of the BC and OM were assumed to be $1.95 - 0.79i$ (Bond and Bergstrom, 2006) and $1.43 - 0i$ (Schmid et al. 2009), respectively.

The calculated E_{abs} values increased with temperature and reached 1.10 and 1.12 at 400°C when idling and driving at 70 km/h, respectively, as indicated by the solid lines in Figure 26. The differences in the estimated and observed E_{abs} values do not necessarily mean that the OM is externally mixed with the BC, because the core-shell Mie theory overestimates E_{abs} values when particles are non-spherical and/or the core is located at the edges of the particles (e.g. Adachi et al. 2010). The possible contributions of change in particle shape during heating also cannot be ruled out. However, the decrease in NFR as the heater temperature increased suggests that at least a part of the OM is externally mixed with the BC, because the total number of particles should not decrease with heating if all of the OM is internally mixed with the BC. In addition, the bimodal size distributions observed at temperatures greater than 200°C when idling (Figure 24, upper panel) suggest that at least two different types of particles existed. Nanoparticles with diameters less than ~20 nm, which increased after heating to 400°C, may be refractory cores of oil-derived elements, such as Ca, K, Fe, and Zn (e.g. Miller et al. 2007, Rönkkö et al. 2007, Fushimi et al. 2011).

Using the same procedure that used for the JE-05 mode [eq. (4)], the contribution of light absorption by OM, which evaporated below 300°C, to total aerosol light absorption at 405 nm was estimated to be 4 ± 12 and 0 ± 16% when idling and driving at 70 km/h, respectively. These results, as well as the observed temperature dependence of the AAE values, suggest that the contribution of light absorption by OM during constant-driving mode was minimal. The smaller contribution of light absorption by OM during the constant-driving compared to that during the high-speed driving period in JE-05 mode may be due to the lower emission of OM during constant-speed driving, although the influence of differences in the chemical compositions of OM on light absorption cannot be ruled out.

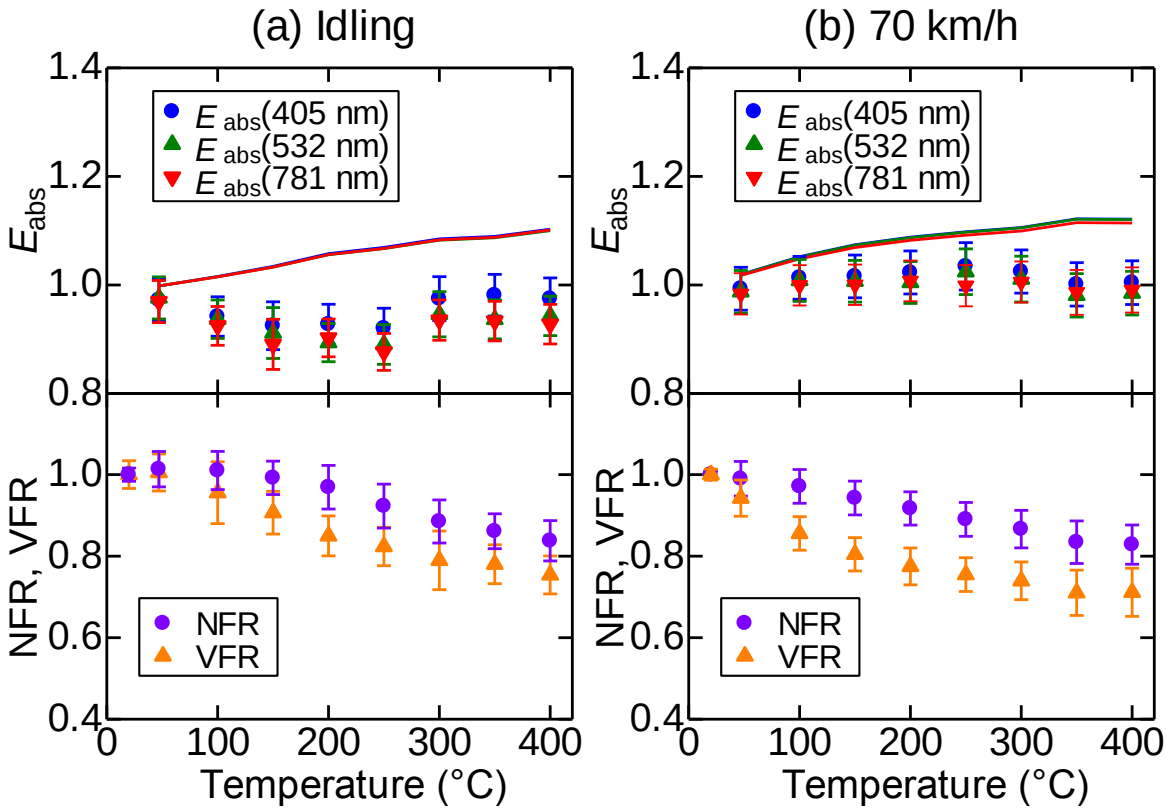

Figure 26. Heater temperature dependence of the (upper panels) absorption enhancement factor (E_{abs}) at 405, 532, and 781 nm and (lower panels) number and volume fraction remaining during constant-speed driving mode: (a) idling and (b) driving at 70 km/h. Solid lines in the upper panel show absorption enhancement factor ($E_{abs,cal}$) at 405 (blue), 532 (green), and 781 (red) nm calculated using the core-shell Mie theory [eq. (5)], assuming that all non-refractory materials evaporated between each temperature and 400°C coated the BC.

Chapter 4

Conclusions

The optical properties of the DEP emitted from a diesel engine vehicle running on a chassis dynamometer in transient driving mode (JE-05) and constant-speed modes (idling and at 70 km/h) were examined using PASS-3. By measuring the change in optical properties after passing the DEP through a heater at temperatures up to 300°C (transient driving mode) or 400°C (constant-speed modes), enhancement of light absorption due to the coating of OM on the BC and the contribution of light-absorbing OM were determined.

Solubility-based analysis showed that the OM accounted for an average of ~40 and ~35% of the total mass concentration of DEP during the JE-05 and constant driving modes, respectively. For the JE-05 mode, most of the organics were emitted during the high-speed driving period between 1480 and 1650 sec (especially, just after completing hard acceleration to high-speed at ~80 km/h and just after initiating deceleration from high-speed) based on analyses of chemical compositions using Q-AMS. However, no enhancement of light absorption due to OM coating on the BC was observed for either JE-05 (including the high-speed driving period) or the constant-speed modes. These results suggest that the lensing effect for fresh DEP is small, even if OM was emitted with BC simultaneously, possibly because the BC was mainly externally mixed with the OM or was located at the edges of particles, even if the OM and BC components were internally mixed in the same particles.

The AAE(405 nm/532 nm) values at heater temperatures of 20 and 47°C also increased from 1.16 ± 0.27 and 1.16 ± 0.24 during the other periods to 1.84 ± 0.32 and 1.64 ± 0.30, respectively, during the high-speed driving period of the JE-05 mode, when greater amount of OM was emitted. The contribution of light absorption by the OM to the total light absorption at 405 nm during the high-speed driving period was estimated to be 20 ± 7%. Although the OM was emitted in substantial amounts under certain conditions, a large amount of OM was emitted; therefore, even emissions during short bursts could contribute to the radiation balance at wavelengths less than ~400 nm.

Further studies on the lensing effect and light-absorbing properties of OM for various types of diesel vehicles are required for a full understanding of the optical properties of DEP. Experimental studies at shorter wavelengths are needed to evaluate the influence of particle light absorption on the photochemistry of the atmosphere.

Acknowledgement

I am grateful to H. Yamada (NTSEL), S. Inomata (NIES), K. Tonokura (University of Tokyo), K. Watanabe (NTSEL) and T. Yamasaki (Nagoya University) for their kind support on experiments.

I am also grateful to Yasusuke Kojima and Hiroshi Sasago for their kind support on the laboratory experiments. I would like offer special thanks to my supervisors Tomoki Nakayama and Yutaka Matsumi for providing me direction during my doctoral course and fruitful comments on my research. I offer best wishes to students of the Matsumi laboratory. I would like to thank all my Japanese friends for their pleasant company through my life in Japan. I especially thank the family of Hirohiko Fukuda for their encouragement.

Finally, I am grateful to my parents and wife for their unflinching support and encouragement.

References

Abo Riziq, A., Erlick, C., Dinar, E., Rudich, Y., 2007. Optical properties of absorbing and non-absorbing aerosols retrieved by cavity ring down (CRD) spectroscopy, Atmos. Chem. Phys., 7, 1523-1536.

Adachi, K., Chung, D. H., Buseck P. R., 2010. Shapes of soot aerosol particles and implications for their effects on climate, J. Geophys. Res. 115, D15206, doi:10.1029/2009JD01288.

Adler, G., Abo Riziq, A., Erlick, C., Rudich, Y., 2010. Effect of intrinsic organic carbon on the optical properties of fresh diesel soot, Proc. Natl. Acad. Sci. USA 107, 6699–6704.

Alam M.S., Rezaei S.Z., Stark C.P., Liang Z., Xu H.M., Harrison R.M., 2016. The characterisation of diesel exhaust particles – composition, size distribution and partitioning, Faraday Discuss., 2016, 189, 69, doi: 10.1039/c5fd00185d

Andreae, M. O., Gelencsér, A., 2006. Black carbon or brown carbon? The nature of light-absorbing carbonaceous aerosols. Atmos. Chem. Phys. 6, 3131-3148.

Andreae, M.O., 2009. A new look at aging aerosols. Science 326, 1493, doi:10.1126/science. 1183158

Baynard, T., Lovejoy, E. R. , Pettersson, A., Brown, S. S., Lack, D., Osthoff, H., Massoli, P., Ciciora, S., Dube, W. P., Ravishankara, A. R., 2007. Design and applications of a pulsed cavity ring-down aerosol extinction spectrometer for field measurements, Aerosol Sci. Technol., 41, 447-462.

Bohren, C.F., Huffman, D.R., 1983. Absorption and scattering of light by small particles. John-Wiley & Sons. Inc., New York.

Bond, T.C., Bergstrom, R.W., 2006. Light absorption by carbonaceous particles: An investigative review. Aerosol Sci. Technol. 40, 27-67.

Bond, T.C., Habib, G., Bergstrom, R.W., 2006. Limitations in the enhancement of visible light absorption due to mixing state, J. Geophys. Res. 111, D20211, doi:10.1029/2006jd007315.

Bond, T.C., Doherty, S.J., Fahey, D.W., Forster, P.M., Berntsen, T., DeAngelo, B.J.,

Flanner, M.G., Ghan, S., Kärcher, B., Koch, D., Kinne, S., Kondo, Y., Quinn, P.K., Sarofim, M.C., Schultz, M.G., Schulz, M., Venkataraman, C., Zhang, H., Zhang, S., Bellouin, N., Guttikunda, S.K., Hopke, P.K., Jacobson, M.Z., Kaiser, J.W., Klimont, Z., Lohmann, U., Schwarz, J.P., Shindell, D., Storelvmo, T., Warren, S.G., Zender, C.S., 2013. Bounding the role of black carbon in the climate system: A scientific assessment. J. Geophys. Res. 118, 5380-5552, doi:10.1002/jgrd.50171.

Cappa, C.D., Onash, T.B. Massoli, P., Worsnop, D.R., Bates, T.S., Cross, E.S., Davidovits, P., Hakala, J., Hayden, K.L., Jobson, B.T., Kolesar, K.R., Lack, D.A., Lerner, B.M., Li, S.–M., Mellon, D., Nuaaman, I., Olfert, J.S, Petäjä, T., Quinn, P.K., Song, C., Subramanian, R., Williams, E.J., Zaveri, R.A., 2012. Radiative absorption enhancements due to the mixing state of atmospheric black carbon, Science 337, 1078-1081.

Chan, T. W., Brook, J. R., Smallwood, G. J., and Lu, G., 2011. Time-resolved mesurements of black carbon light absorption enhancement in urban and near-urban locations of southern Ontarion, Canada, Atmos. Chem. Phys., 11, 10407-10432, doi: 10.5194/acp-11-10407-2011.

Docherty, K. S., M. Jaoui, E. Corse, J. L. Jimenez, J. H. Offenberg, M. Lewandowski, and T. E. Kleindienst, 2013. Collection efficiency of the aerosol mass spectrometer for chamber-generated secondary organic aerosols, Aerosol Sci. Technol., 47, 294–309.

Fushimi, A., Saitoh, K., Fujitani, Y., Hasegawa, S., Takahashi, K., Tanabe, K., Kobayashi, S., 2011. Organic-rich nanoparticles (diameter: 10-30 nm) in diesel exhaust: Fuel and oil contribution based on chemical composition. Atmos. Environ. 45, 6326-6336.

Hadley, O. L., Corrigan, C. E., Kirchstetter, T. W., Modified thermal-optical analysis using spectral absorption selectivity to distinguish black carbon from pyrolized organic carbon. Environ. Sci. Technol. 42, 8459-8464.

Healy, r. M., Wang, J. M. Jeong, C-H., Lee, A. K. Y., Willis, M.D., Jaroudi, E., Zimmerman, N., Hilker, N., Murphy, M., Eckhardt, S., Stohl, A., Abbatt, J. P. D., Wenger, J. C., and Evans, G. J., 2015. Light-absorbing properties of ambient black carbon and brown carbon from fossil fuel and biomass burning sources, J. Geophy. Res.-Atmos., 120, 6619-6633, doi:10.1002/2015JD023382.

Huffman, J.A., Ziemann, P.J., Jayne, J.T., Worsnop, D.R., Jimenez, J.L., 2008. Development and characterization of a fast-stepping/scanning thermodenuder for chemically-resolved aerosol volatility measurements, Aerosol Sci. Technol. 42, 395-407.

Inomata, S., Tanimoto, H., Fujitani, Y., Sekimoto, K., Sato, K., Fushimi, A., Yamada, H.,Hori, S., Kumazawa, Y., Shimono. A., Hikida, T., 2013. On-line measurements of gaseous nitro-organic compounds in diesel vehicle exhaust by proton-transfer reaction mass spectrometry. Atmos. Environ. 73, 195-203.

Jacobson, M.Z., 1999. Isolating nitrated and aromatic aerosols and nitrated aromatic gases as sources of ultraviolet light absorption, J. Geophys. Res. 104, 3527–3542.

Kondo, Y., Sahu, L., Kuwata, M., Miyazaki, Y., Takegawa, N., Moteki, N., Imaru, J., Han, S., Nakayama, T., Kim Oanh, N. T., Hu, M., Kim, Y. J., Kita, K., 2009. Stabilization of the mass absorption cross section of black carbon for filter-based absorption photometry by the use of a heated inlet, Aerosol Sci. Technol. 43, 741-756.

Knox A., Evans, G.J., Brook, J.R., Yao, X., Jeong, C.-H., Godri, K. J., Sabaliauskas, K., and Slowik, J. G., 2009. Mass absorption cross-section of ambient black caron aerosol in relation to chemical age, Aerosol Sci. Technol., 43, 522-532, doi:10.1080/02786820902777207,.

Lack, D.A., Cappa, C.D., 2010. Impact of brown and clear carbon on light absorption enhancement, single scatter albedo and absorption wavelength dependence of black carbon, Atmos. Chem. Phys. 10, 4207–4220.

Lack D.A., Cappa C.D., Covert D.S. Baynard T., Massoli P. Sierau B., Bates T.Y., Quinn P.K., Lovejoy E.R., Ravishankara A.R., 2008. Bias in Filter-Based Aerosol Light Absorption Measurements Due to Organic Aerosol Loading: Evidence from Ambient Measurements, Aerosol Sci. Technol., 42:12, 1033-1041, doi: 10.1080/02786820802389277

Lang-Yona, N., Rudich, Y., Segre, E., Dinar, E., Abo-Riziq, A., 2009. Complex refractive indices of aerosols retrieved by continuous wave-cavity ring down aerosol spectrometer, Anal. Chem., 81, 1762-1769.

Lewis, K., Arnott W.P., Moosmüller H., and Wold C.E. 2008, Strong spectral variation of biomass smoke light absorption and single scattering albedo observed with a novel

dual-wavelength photoacoustic instrument, J. Geophys. Res., 113, D16203, doi:10.1029/2007JD009699.

Maricq, M.M., 2007. Chemical characterization of particulate emissions from diesel engines: a review. J. Aerosol Sci. 38, 1079-1118.

Mathseon, L. A., Saunderson, J. L., 1952. Optical and electrical properties of polystyrene, In R. H. Boundy, R. F. Boyer (Eds.), Styrene, its polymers, copolymers and derivatives (pp. 517–573), New York, Reinhold Publishing Corp.

Miller, A.L., Stipe, C.B., Habjan, M.C., Ahlstrand, G.G., 2007. Role of lubrication oil in particulate emissions from a hydrogen-powered internal combustion engine. Environ. Sci. Technol. 41, 6828-6835.

Middlebrook, A. M., R. Bahreini, J. L. Jimenez, M. R. Canagaratna, 2012. Evaluation of composition-dependent collection efficiencies for the Aerodyne Aerosol Mass Spectrometer using field data, Aerosol Sci. Technol., 46, 258–271.

Mohr, C., Lopez-Hilfiker, F.D., Zotter, P., Prévôt, A.S., Xu, L., Ng, N.L., Herndon, S.C., Williams, L.R., Franklin, J.P., Zahniser, M.S., Worsnop, D.R., Knighton, W.B., Aiken, A.C., Gorkowski, K.J., Dubey, M.K., Allan, J.D., Thornton, J.A., 2013. Contribution of nitrated phenols to wood burning brown carbon light absorption in Detling, United Kingdom during winter time. Environ. Sci. Technol. 47, 6316-6324.

Moosmüller, H., Arnott, W.P., Rogers, C.F., Bowen, J.L., Gillies, Pierson, W.R., Collins, J.F, Durbin, T.D., Norbeck, J.M., 2001. Time-resolved characterization of diesel particulate emissions. 2. Instruments for elemental and organic carbon measurements. Environ. Sci. Technol. 35, 1935–1942.

Moosmüller, H., Chakrabarty, R.K., Arnott, W.P., 2009. Aerosol light absorption and its measurement: A review. J. Quant. Spectrosc. Radiat. Transfer 110, 844-878.

Myhre, G., D. Shindell, F.-M. Bréon, W. Collins, J. Fuglestvedt, J. Huang, D. Koch, J.-F. Lamarque, D. Lee, B. Mendoza, T. Nakajima, A. Robock, G. Stephens, T. Takemura and H. Zhang, 2013: Anthropogenic and Natural Radiative Forcing. In: Climate Change 2013: The Physical Science Basis. Contribution of Working Group I to the Fifth Assessment Report of the Intergovernmental Panel on Climate Change (Stocker, T.F., D. Qin, G.-K. Plattner, M. Tignor, S.K. Allen, J. Boschung, A. Nauels, Y. Xia, V. Bex and P.M. Midgley (eds.)). Cambridge University Press, Cambridge, United Kingdom and New York, NY, USA.

Nakayama, T., Matsumi, Y., Sato, K., Imamura, T., Yamazaki, A., Uchiyama, A., Laboratory studies on optical properties of secondary organic aerosols generated during the photooxidation of toluene and the ozonolysis of α-pinene, 2010, J. Geophys. Res., 115, D24204, doi:10.1029/2010JD014387.

Nakayama, T., Suzuki, H., Kagamitani, S., Ikeda, Y., Uchiyama, A., Matsumi, Y., 2015. Characterization of a three wavelength photoacoustic soot spectrometer (PASS-3) and a photoacoustic extinctiometer (PAX), J. Meteor. Soc. Japan, 93, 285-308.

Nakayama, T., Sato, K., Matsumi, Y., Imamura, T., Yamazaki, A., Uchiyama, A., 2013. Wavelength and NO_x dependent complex refractive index of SOAs generated from the photooxidation of toluene. Atmos. Chem. Phys. 13, 531-545.

Nakayama, T., Ikeda, Y., Sawada, Y., Setoguchi, Y., Ogawa, S., Kawana, K., Mochida, M., Ikemori, F., Matsumoto, K.and Matsumi Y., 2014. Properties of light-absorbing aerosols in the Nagoya urban area, Japan, in August 2011 and January 2012: Contributions of brown Carbon and lensing effect. J. Geophys. Res., 119, 12721-12739, doi:10.1002/2014JD021744.

Pöschl, U.: Aerosol particle analysis: challenges and progress, Anal. Bioanal. Chem., 375, 30–32, 2003.

Pettersson, A., Lovejoy, E. R., Brock, C. A., Brown, S. S., Ravishankara, A. R., 2004. Measurement of aerosol optical extinction at 532 nm with pulsed cavity ring down spectroscopy, J. Aerosol Sci., 35, 995-1011.

Rönkkö, T., Virtanen, A., Kannosto, J., Keskinen, J., Lappi, M., Pirjola, L., 2007. Nucleation mode particles with a nonvolatile core in the exhaust of a heavy duty diesel vehicle. Environ. Sci. Technol. 41, 6384-6389.

Rian Y., James G. R., Michael R. Z., and Christopher D. Z., 2016. Measured wavelength- dependent absorption enhancement of internally mixed black carbon with absorbing and nonabsorbing, Environ. Sci. Technol. 2016, 50, 7982-7990.

Ueda, S., Nakayama, Y., Taketani, F., Adachi, K., Matsuki, A., Iwamoto, Y., Sadanaga, Y., and Matsumi Y., 2016. Light absorption and morphological properties of soot-containing aerosols observed at an East Asian outflow site, Noto Peninsula., Atmos. Chem. Phys., 16, 2525-2541., doi: 10.5194/acp-16-2525-2016.

Schmid, O., Chand, D., Karg, E., Guyon, P., Erank, G.P., Swietlicki, E., Andreae, M.O.,

2009. Derivation of the density and refractive index of organic matter and elemental carbon from closure between physical and chemical aerosol properties. Environ. Sci. Technol. 41, 6384-6389.

Schnaiter, M., Linke, C., Möhler, O., Naumann, K.H., Saathoff, H., Wagner, R., Schurath, U., Wehner, B., 2005. Absorption amplification of black carbon internally mixed with secondary organic aerosol, J. Geophys. Res. 110, D19204, doi: 10.1029/2005jd006046.

Shiraiwa, M., Kondo, Y., Iwamoto, T., Kita, K., 2010. Amplification of light absorption of black carbon by organic coating, Aerosol Sci. Technol. 44, 46–54.

Swarup C., Claudio M., Kyle G., Allison, C. A. and Manvendra K. D., 2013. Morphology and micing state of individual freshly emitted wildfire carbonaceous particles. Nat. Commun, 6:8435, doi:10.1013/ncomms9435.

Washenfelder, R. A., Flores, J. M., Brock, C. A., Brown, S. S., Rudich, Y., 2013. Broadband measurements of aerosol extinction in the ultraviolet spectral region, Atmos. Meas. Tech., 6, 861–877.

Yamada, H., Misawa, K., Suzuki, D., Tanaka, K., Matsumoto, J., Fujii, M., Tanaka, K., 2011. Detailed analysis of diesel vehicle exhaust emissions: nitrogen oxides, hydrocarbons and particulate size distribution. Proc. Combust. Inst. 33, 2895-2902.

Yamamoto, Y., Kambe, Y., Yamada, H., Tonokura, K., 2012. Measurement of volatile organic compounds in vehicle exhaust using single-photon ionization time-off light mass spectrometry. Anal. Sci. 28, 385-390.

Zhang, X., Lin, Y.-H., Surratt, J.D., Zotter, P., Prévôt, A.S.H., Weber, R.J., 2011. Light-absorbing soluble organic aerosol in Los Angeles and Atlanta: A contrast in secondary organic aerosol. Geophys. Res. Lett., 38, L21810, doi:10.1029/2011gl049385.

Zhang, X., Lin, Y.-H., Surratt, J.D., Weber, R.J., 2013. Source, composition and absorption Ångström exponent of light-absorbing organic components in aerosol extracts from the Los Angeles basin. Environ. Sci. Technol. 47, 3685-3693.

Zhong, M., Jang, M., 2011. Light absorption coefficient measurement of SOA using a UV-Visible spectrometer connected with an integrating sphere, Atmos. Environ. 45, 4263–4271.

Zhong, M., Jang, M., Oliferenko, A., Pillai, G.G., Katritzky, A.R., 2012. The SOA

formation model combined with semiempirical quantum chemistry for predicting UV-Vis absorption of secondary organic aerosols, Phys. Chem. Chem. Phys. 14, 9058–9066.